UNIVERSIDADE DE LISBOA
FACULDADE DE CIÊNCIAS

A computational study of surface accumulation and exploration of chiral active particles

" Documento Definitivo"

Doutoramento em Física e Astrofísica

Danne van Roon

Tese orientada por:
Nuno Araújo e Margarida Telo da Gama

Documento especialmente elaborado para a obtenção do grau de doutor

2024

UNIVERSIDADE DE LISBOA
FACULDADE DE CIÊNCIAS

A computational study of surface accumulation and exploration of chiral active particles

Doutoramento em Física e Astrofísica

Danne van Roon

Tese orientada por:
Nuno Araújo e Margarida Telo da Gama

Júri:
Presidente:

- José Manuel de Nunes Vicente e Rebordão, investigador Coordenador e membro do Conselho Científico da Faculdade de Ciências da Universidade de Lisboa

Vogais:

- Doutor Hartmut Löwen, Chair Professor do Institut für Theoretische Physik II Soft Matter da Heinrich-Heine-Universität Düsseldorf
- Doutor Clemens Bechinger, Full Professor do Physics da Universität Konstanz
- Doutor José Maria Cantista de Castro Tavares, Professor Coordenador do Instituto Superior de Engenharia de Lisboa do Instituto Politécnico de Lisboa
- Doutor Nuno Miguel Azevedo Machado de Araújo, Professor Associado com Agregação da Faculdade de Ciências da Universidade de Lisboa (orientador)

Documento especialmente elaborado para a obtenção do grau de doutor

Doutoramento financiado pela European Commission
Horizon 2020 research and innovation program and from the
Portuguese Foundation for Science and Technology (FCT)

2024

Acknowledgements

Whilst working on my research I have received wonderful support without which this thesis would never have been possible. First of all, I would like to thank my doctoral advisors Nuno and Margarida for initiating the project, and for their scientific input and guidance during its development. Fondly will I remember our animated discussions stretching the odd lunch a bit. Nuno thank you especially for our weekly discussions, typically beginning with science and ending with sailing, I hope that we may sail together one day. I also would like to thank Giorgio, firstly for his kindness and advice, and then for his critical feedback, which vastly improved the quality of our work.

My collegues at the CFTC amongst others, Andrè, Iñaki, Rafael, Henrique, Thomás, Manuel, Vasco, Júlio, Rodrigo, Christóvão and João for the warm, pretentionless and genuine atmosphere.

Angela Antunes for helping me to overcome the wall of burocracy, without whom I would probably still be trying to enrol in the first year of the Phd program.

Thanks to my friends and flatmates in Lisbon, Eva, Lukas and Diogo who made me feel "em casa" and Lukas also for his unbridled curiosity and enthusiasm for Mushrooms amongst other things.

To Nicolas, Chris, Beatriz, Eli, Paz, Nat, Antony and Lise for the unforgettable sundowns at the crags, I hope there will be more. To Matteo, what a time we had discussing "os Portugueses" (ft. C Daniel).

The Netherlands to which I am returning, is shaped by strong and warm friendships. Thank you Tim, Melle, Coen and Loekie. I will be glad to to see you more often, and thank you for enabling a less abstract and more playful world. I am fortunate that my life may include some wonderful people. Hieke with whom I spend many a beautiful day, even during the gloomy times of Covid we found joy. Geert as a good friend, always able to challenge my mind. Eyzo who with his unbounded creativity and being always brightens me up one way or another. Vitaly

for the times we spend together in Paris, even now as I am writing this. Reimer with whom I share a friendship as long as I can remember.

I conclude with a sense of gratitude, to be born in the family of Petra, Frans, Jippe en Mari, which is one of unconditional love and support, well beyond this thesis.

Finally, to my love Pippi who inspires me and is my home, I know you will always have my back.

Abstract

Biological and man-made active particles (microswimmers when hydrodynamics are considered) often move in complex crowded environments where they encounter boundaries such as surfaces or obstacles. Recently it was shown experimentally that the interaction of active particles with boundaries is determined primarily by steric forces and short-ranged hydrodynamics. In the first chapter of this thesis, we consider solely steric interactions and study numerically the role of disorder in the transport dynamics of chiral active particles on surfaces with obstacles. We consider different densities of regularly spaced obstacles and distinct types of disorder: noise in the dynamics of the particle, quenched noise in the positions of the obstacles as well as obstacle size polydispersity. We show that, depending on the type and strength of the disorder, the presence of obstacles can either enhance or hinder mass transport. In the second chapter, we introduce a three-dimensional model of a microswimmer, where we include hydrodynamics in an effective way, navigating a volume bounded by a top and bottom surface. We describe the swimmer-surface interaction with an effective short-ranged hydrodynamic alignment force, and study numerically the effect of surface texture, modelled by obstacles, on the surface accumulation of chiral and non-chiral microswimmers. We find that, depending on the angular velocity of the swimmer, and the alignment force, obstacles can either hinder or enhance surface accumulation. We discuss potential applications to sorting of microswimmers by their angular velocity.

Keywords — chiral active particles, disorder in transport dynamics, obstacles and surface structure, 3D model of a microswimmer, surface accumulation of bacteria

Resumo

Partículas ativas quirais, sejam elas biológicas ou artificiais, raramente se movem em ambientes homogéneos, mas encontram, em vez disso, heterogeneidade na forma de fronteiras, como paredes de domínio ou poros, e obstruções ou obstáculos da ordem do tamanho da particula. Esforços recentes de investigacão têm-se concentrado em entender os mecanismos (bio)físicos subjacentes às partículas ativas quirais em ambientes heterogéneos. Do ponto de vista fundamental, isso é interessante para compreender e otimizar estratégias de busca em ambientes realistas. Do ponto de vista prático, tal compreensão é crucial para explicar e controlar processos biomedicamente relevantes, como a formação de biofilmes. Além disso, há um potencial significativo e ainda não explorado para possibilitar novas aplicações nanotecnológicas, incluindo, por exemplo, transportadores de carga autopropelidos com aplicações em entrega de medicamentos em tecidos ou remoção de contaminação em solos porosos.

Uma propriedade importante da matéria ativa é a assimetria inerente na interação de partículas ativas com fronteiras. Ao se aproximar de uma fronteira, uma partícula ativa nada na direcão desta, efetivamente ficando 'presa' na fronteira, até que sua direção de movimento aponte para fora da superficie. Ao se afastar de uma fronteira, a partícula mover-se-á livremente até encontrar outra fronteira. Devido a essa assimetria, as partículas ativas tendem a acumular-se perto de fronteiras, mesmo quando são puramente repulsivas. Para partículas passivas, tal acumulação próxima das fronteiras não é observada e exigiria uma interação atrativa. Resultados recentes com *E. coli* perto de uma superfície mostraram que a reorientação média das células em direção paralela à superfície é impulsionada por forças estéricas no contato e hidrodinâmica de curto alcance, com a hidrodinâmica de longo alcance desempenhando apenas um papel secundário. Resultados semelhantes foram obtidos para células de esperma numa superfície, para *E. coli* interagindo com pilares microscópicos e para micropropulsores sintéticos navegando num ambiente de particulas coloidais passivas.

No primeiro capítulo, examinamos numericamente o efeito da desordem (doravante deno-

minada 'ruído') nas interações estéricas na dinâmica de partículas ativas quirais explorando um arranjo periódico de obstáculos, onde introduzimos ruído de maneira controlada. Primeiro, consideramos uma partícula ativa quiral que não sofre nenhuma difusão browniana rotacional na presença de um arranjo periódico de obstáculos. Tipos distintos de ruído são então introduzidos independentemente: 'ruído dinâmico', que determina a reorientação da partícula, e dois tipos de 'ruído quenched', sendo o primeiro a desordem nas posições dos obstáculos, e o segundo a polidispersidade nos tamanhos dos obstáculos.

Para quantificar o efeito dos diferentes tipos de ruído nas propriedades de transporte da partícula ativa, calculamos o coeficiente de difusão efetivo (difusividade) para uma ampla faixa de frações de área (densidades) de obstáculos e intensidades de ruído. Constatamos que a difusividade de uma partícula ativa quiral é fortemente não monótona com o aumento da densidade de obstáculos. Em densidades mais baixas, o transporte de uma partícula ativa quiral é retificado devido à interação da partícula com os obstáculos, afetando as órbitas e permitindo que a partícula explore o espaço. Em densidades mais altas, a partícula não consegue realizar movimento quiral devido às interações constantes com os obstáculos, e a difusividade é reduzida até que as condições sejam adequadas para que o movimento seja canalizado. Quando a intensidade do ruído dinâmico é aumentada, a difusividade aumenta para todas as densidades, exceto as mais altas, o que atribuímos à aleatoridade das órbitas quirais. Além disso, a capacidade da partícula de explorar melhor o espaço torna-se menos dependente dos obstáculos. Em densidades mais altas, o ruído dinâmico suprime o transporte orientado por canais. O ruído 'quenched' introduz desordem na disposição espacial dos obstáculos, resultando em movimento errático, e perturbando o movimento orientado por canais.

No segundo capítulo, introduzimos um modelo 3D para examinar a acumulação na superfície de micropropulsores induzida por forças estéricas e uma força eficaz de alinhamento hidrodinâmico de curto alcance que alinha a direção de propagação dos propulsores ao longo da fronteira mais próxima. Tomamos *E. coli* e células de esperma de touro como exemplos, navegando num volume delimitado por um plano de superfície superior e um inferior, semelhante a um canal de microfluídica. Estudamos o efeito de colocar obstáculos convexos, que têm três vezes o tamanho dos propulsores, aleatoriamente em ambas as superfícies, e examinamos como a acumulação na superfície depende de força de alinhamento e velocidade angular do movimento. Quantificamos essa acumulação na superfície medindo a fração de propulsores próximos às superfícies. Constatamos que a presença de obstáculos sempre reduz a acumulação

de micropropulsores não quirais, já que, ao se alinharem ao longo da fronteira dos obstáculos, os propulsores são direcionados para longe da superfície. À medida que a densidade de obstáculos aumenta, a acumulação na superfície é reduzida. Para micropropulsores quirais, a acumulação pode ser reduzida ou aumentada. Observamos o 'aprisionamento' dinâmico de propulsores, no qual os propulsores se movem em órbitas ao longo da fronteira de um obstáculo, em conformidade com observações experimentais anteriores. Este aprisionamento orbital resulta da interação de alinhamento e do movimento quiral do propulsor e só ocorre se os obstáculos forem pelo menos iguais ao tamanho da órbita. Discutimos como obstáculos podem ser usados para controlar a acumulação de propulsores quirais próximos às superfícies, ajustando cuidadosamente seu tamanho. Além disso, discutimos como obstáculos podem ser empregados para classificar propulsores com base em sua velocidade angular.

Palavras chave — partículas ativas quirais, desordem na dinâmica de transporte, obstáculos e estrutura de superfície, modelo 3D de um micropropulsor, acumulação de bactérias na superfície

Contents

List of Figures

List of Symbols

N number of active particles/swimmers

N_{obstacle} number of obstacles

ρ density of obstacles on surface

L lateral length of the surface plane

σ active particle/swimmer size

σ_{obstacle} obstacle size

D_{R} rotational diffusion constant

D_{T} translational diffusion constant

k_{B} Boltzmann constant

η kinematic viscocity

$\vec{\xi}$ stochastic force

ξ white noise with zero mean and unit variance

x component of the position vector

y component of the position vector

θ orientation in $x - y$ plane

$\vec{v}$ velocity vector

v speed

Ω angular speed

$\vec{p}$ momentum vector

p_0 reference momentum vector amplitude

R_{o} radius swimming orbit chiral active particle/swimmer

t time

τ time scale motility

τ_{R} time scale rotational Diffusion

Δt simulation time step

V potential

F_x x component force (Weeks-Chandler-Anderson potential)

F_y y component force (Weeks-Chandler-Anderson potential)

$\vec{F}_{\text{motile}}$ motile force

$\vec{F}_{\text{surface}}$ surface component force

$\vec{F}_{\text{steric}}$ steric component force

α alignment interaction force strength

β near surface angular velocity (of chiral active particle/swimmer)

r distance between active particle/swimmer and boundary

r_{c} cut off distance

$\mu_{\perp}$ vector perpendicular to boundary closest to active particle/swimmer

ϕ fraction of active particles/swimmers accumulated at surface

ϕ_0 fraction of active particles/swimmers accumulated at smooth surface

Introduction

Active matter systems are able to harvest energy from their environment and drive themselves far from equilibrium. This ability gives rise to a series of novel behaviours that are not observed in systems that are at thermal equilibrium, including accumulation at walls, swarming, motility induced phase separation (MIPS), among many other emergent collective properties [1, 2]. An important example of active matter consists in natural and artificial objects capable of self-propulsion. Clearly the meaning of 'self-propulsion' can be applied very broadly, often animals such as (shoals of) fish or (flocks of) birds, but also drones and centimeter sized robots (e.g. HEXBUGs) are rightly considered active matter [1, 3]. In this thesis however, we will predominantly discuss smaller objects, at the micron scale.

Mechanisms of self-propulsion include external fields (e.g. changing electric and magnetic fields) and local conversion mechanisms such as phoresis where particles are exposed to a chemical, electrostatic or thermal field gradient. A different kind of active matter are biological swimmers such as algae, bacteria including Echerichia coli (E. Coli), or sperm cells, self propelling by means of a flagellum (sperm cell) or a bundle of flagella (E. Coli) [4].

For any swimming mechanism, swimming along a straight line is the exception rather than the rule. In fact, 'ideal straight swimming' occurs only if the left-right symmetry relative to the direction of propulsion is conserved, even small deviations from this symmetry will destabilize any straight motion, resulting in 'chiral' motion. The term 'chiral' was coined by Lord Kelvin in 1983 to define an object that is distinguishable from its mirror image, that is if its image in a plane mirror cannot be brought to coincide with itself. Many active particles have chiral shapes, or an anisotropy in their propulsion mechanism, resulting in chiral trajectories [4–6]. Typical chiral trajectories resemble circles when the active particle is confined to a surface (2D), or helices when it can move freely in the bulk (3D) [7]. Alternatively, chirality can be induced by external fields, a magnetic field perpendicular to the plane of motion exerting a torque on the particles would result in chiral motion. Other mechanisms depend on hydrodynamic interac-

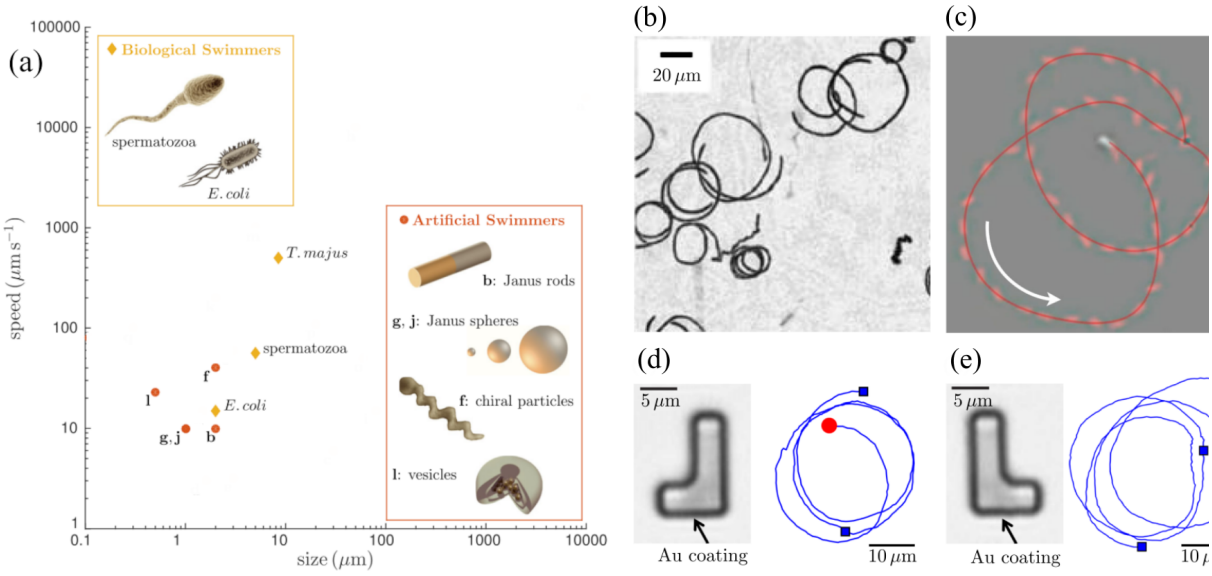

Figure 1: (a) Active swimmers at the micron scale. The vertical axes denotes the speed of the swimmer, the horizontal axes its size. (b-e) Chiral swimmers. (b) Video microscopy images showing E. coli bacteria swimming in circular trajectories near a glass surface. (c) Circular trajectories of E. coli bacteria swimming over liquid-air interfaces. (d,e) L shaped artificial microswimmers driven by self-diffusiophoresis: in each plot, the red bullet corresponds to the initial particle position and the two blue squares to its position after 1 and 2 minutes. The insets show microscope images of two different swimmers with the Au coating (not visible in the bright-field image) indicated by an arrow. Image reproduced from C. Bechinger, R. Di Leonardo, H. Löwen, C. Reichhardt, G. Volpe and G. Volpe, *Reviews of Modern Physics*, 2016, **88**, 045006.

tions of the swimmer with an interface or wall, of which the circular swimming of E. coli near a surface is a paradigmatic example.

When modeling micron scale active matter, there are distinct approaches [8]. The first category of models consists of what are known as ”dry” models, which describe solely the equations of motion for active particles. ”Dry” models are naturally used to describe active systems which do not involve a liquid solvent, but are also often used as a simplified description representing a solvent as an effective hydrodynamic force or thermal bath. The second category consists of ”wet” models, which include the interaction with a solvent by means of a explicit hydrodynamic description. Then there are continuum models for systems of many active particles. In this thesis, we will work with ”dry” models.

One of the simplest ”dry” models is the active Brownian particle (ABP). In this model, the mechanism leading to self-propulsion, which results from the interaction of the active particle with its solvent, is not explicitly described, but replaced with an effective driving force that propels the particle forward. Due to its relative simplicity, the ABP model is intuitive to work with and widely used. Despite its simplicity, it represents well the dynamics of many different active systems, including natural swimmers, such as bacteria, algi and sperm, and synthetic

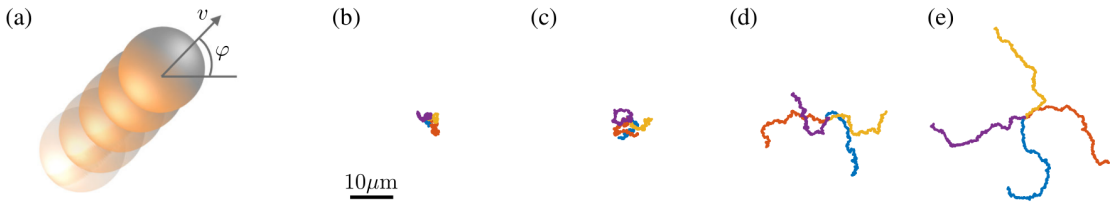

Figure 2: Active Brownian particles in two dimensions. (a) An active Brownian particle in water ($R = 1$ μm), with velocity v and orientation θ. The particle undergoes translational and rotational Brownian diffusion. The resulting trajectories are shown for different velocities (b) v = 0 μm s^{-1}, (c) v = 1 μm s^{-1} , (d) v = 2 μm s^{-1}, and (e) v = 3 μm s^{-1}. As the velocity increases, the particle covers a longer distance before its direction of motion is randomized. Four different 10 s trajectories are shown for each value of velocity. Image reproduced from C. Bechinger, R. Di Leonardo, H. Löwen, C. Reichhardt, G. Volpe and G. Volpe, *Reviews of Modern Physics*, 2016, **88**, 045006.

particles with different shapes and propulsion mechanisms [8, 9].

The ABP model

Let us consider an ABP of size (radius) $R = 1$ μm, with velocity v, if we observe it with a microscope, we will see the particle moving above the flat glass surface of a microscope slide, the direction of motion of the particle randomly changing due to interactions with the solvent molecules surrounding the particle. If we assume the film of fluid to be sufficiently thin, the movement of the particle can be considered to be confined to the horizontal plane (2D). The translational diffusion constant of the ABP is

$$D_{\mathrm{T}} = \frac{k_{\mathrm{B}}T}{6\pi\eta R}, \tag{1}$$

where k_{B} is the Boltzmann constant, T is the absolute temperature, and η is the fluid viscosity. The rotational diffusion constant for the ABP is

$$D_{\mathrm{R}} = \frac{k_{\mathrm{B}}T}{8\pi\eta R^3}, \tag{2}$$

such that on average we will see that the ABP will move along the direction of its initial orientation for a typical time $\tau_{\mathrm{R}} = D_{\mathrm{R}}^{-1}$, covering a finite persistence length,

$$l = v\tau_{\mathrm{R}}. \tag{3}$$

From the expression for the diffusion constants it becomes clear that for larger particles the trajectory becomes more deterministic as the diffusion constants (and thus the randomization of

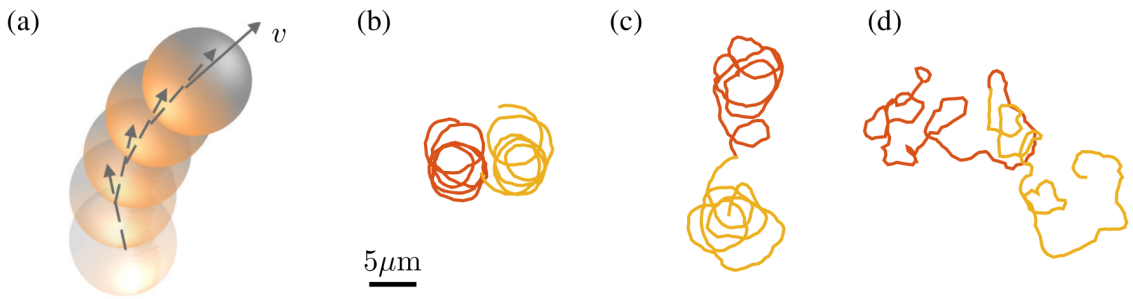

Figure 3: Chiral active Brownian motion in two dimensions. (a) A two-dimensional chiral active Brownian particle with velocity v and angular velocity Ω. The trajectory of the particle continuously deviates from what would be a straight trajectory, resulting in circular motion. (b)–(d) Sample trajectories of chiral active Brownian particles moving clockwise (red) and anticlockwise (yellow). Particles with v = 30 μm s^{-1} , $\Omega = 10$ rad s^{-1}, and different sizes (radii) [R = 1000, 500, and 250 nm for (b), (c), and (d), respectively]. As the particles decrease in size, the trajectories are less determinisitic, because the rotational diffusion scales according to R^{-3}. Image reproduced from C. Bechinger, R. Di Leonardo, H. Löwen, C. Reichhardt, G. Volpe and G. Volpe, *Reviews of Modern Physics*, 2016, **88**, 045006.

the trajectory) scale according to R^{-1} (D_{T}) and R^{-3} (D_{R}). Assuming the solvent to be water at 293K, the diffusion constants work out to be $D_{\mathrm{T}} \approx 0.1$ μm²/s and $D_{\mathrm{R}} \approx 0.2\ \mathrm{rad}^2/\mathrm{s}$.

The motion of the ABP is described by the overdamped Langevin equations in two dimensions,

$$\begin{cases} \dot{x} = v\cos(\theta) + \sqrt{2D_{\mathrm{T}}}\,\xi_x, \\ \dot{y} = v\sin(\theta) + \sqrt{2D_{\mathrm{T}}}\,\xi_y, \\ \dot{\theta} = \sqrt{2D_{\mathrm{R}}}\,\xi_\theta, \end{cases} \tag{4}$$

where x, y denote the position of the particle, θ is its orientation in the plane, and ξ_x, ξ_y and ξ_θ represent independent white noise with zero mean and variance one. Fig. (2) displays some example trajectories of an ABP. In the case of a chiral particle, an angular drift term Ω is included to account for the chirality,

$$\begin{cases} \dot{x} = v\cos(\theta) + \sqrt{2D_{\mathrm{T}}}\,\xi_x, \\ \dot{y} = v\sin(\theta) + \sqrt{2D_{\mathrm{T}}}\,\xi_y, \\ \dot{\theta} = \Omega + \sqrt{2D_{\mathrm{R}}}\,\xi_\theta. \end{cases} \tag{5}$$

In Fig. (3) some example trajectories of a chiral ABP are presented. From equations (4) and (5) we can obtain the mean squared displacement (MSD) of the ABP in an homogeneous environment. In [10] the MSD is calculated

$$\mathrm{MSD}(t) = \left[4D_{\mathrm{T}} + 2v^2\tau_{\mathrm{R}}\right]t + 2v^2\tau_{\mathrm{R}}^2\left[e^{-t/\tau_{\mathrm{R}}} - 1\right], \tag{6}$$

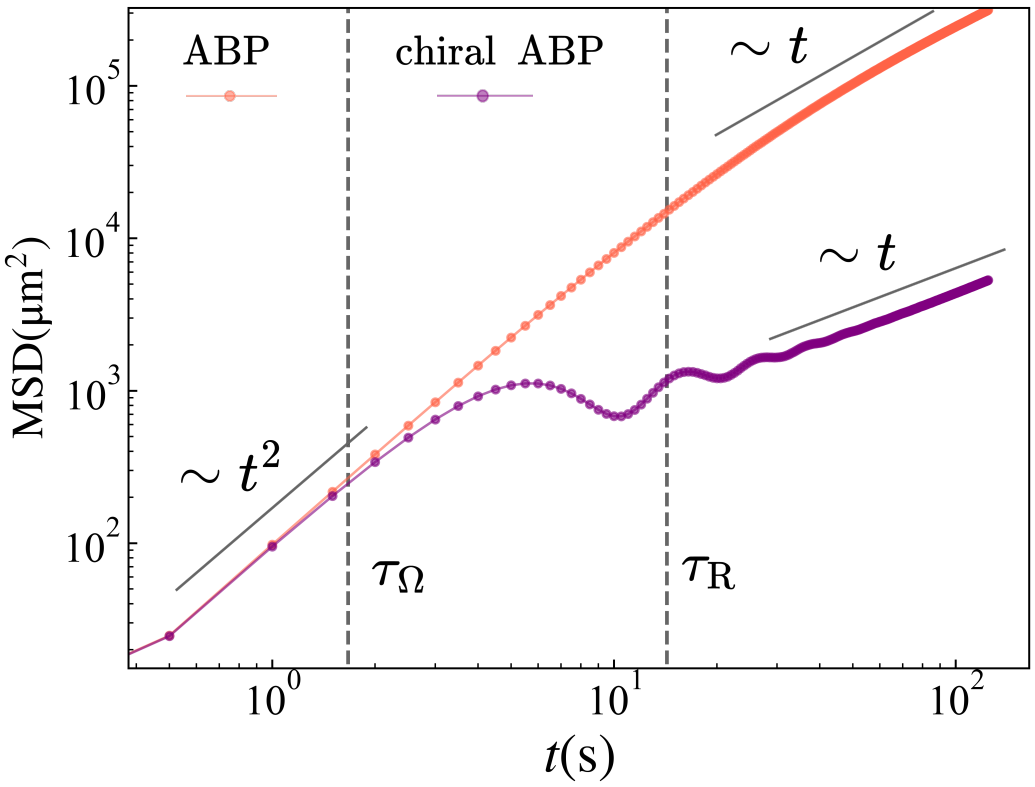

Figure 4: MSD for an ABP with velocity $v = 6\ \mu m/s$ and a chiral ABP with velocity $v = 6\ \mu m/s$ and angular velocity $\Omega = 1\ \mathrm{rad}/s$. The MSD for an ABP is ballistic when $t < \tau_R$, and diffusive at long time scales $t >> \tau_R$, for a chiral ABP the MSD is ballistic when $t < \tau_\Omega$ and diffusive when $t >> \tau_R$.

for small times, around $t = 0$ the equation reduces to a quadratic or ballistic regime

$$\mathrm{MSD}(t) \sim 4D_{\mathrm{T}}t + v^2t^2, \tag{7}$$

for large times, $t >> \tau_{\mathrm{R}}$, a diffusive regime is recovered

$$\mathrm{MSD}(t) \sim \left[4D_{\mathrm{T}} + 2v^2\tau_{\mathrm{R}}\right]t. \tag{8}$$

The ballistic regime results from the ABP performing persistent motion, and is determined by τ_{R}, the typical time it takes for the persistent motion of the ABP to be randomized. For the chiral ABP, an expression for the MSD is computed in [11], the resulting expression

$$\mathrm{MSD}(t) = \frac{2v^2}{D_R^2 + \Omega^2}\left[(\Omega^2 - D_R^2 + D_{\mathrm{R}}\left[D_{\mathrm{R}}^2 + \Omega^2\right]t) + e^{-D_{\mathrm{R}}t}(D_R^2 - \Omega^2)\cos(\Omega t) - 2\Omega D_{\mathrm{R}}\sin(\Omega t)\right]. \tag{9}$$

Also for small times, the expression reduces to a ballistic one

$$\text{MSD}(t) \sim v^2 t^2, \tag{10}$$

and for large times, $t >> \tau_{\text{R}}$, a diffusive expression is recovered

$$\text{MSD}(t) \sim 2v^2 D_{\text{R}}^2 t. \tag{11}$$

For a chiral ABP, the direction of motion is determined by the angular velocity and rotational diffusion. The smallest of the time scales $\tau_{\text{R}} = \frac{1}{D_{\text{R}}}$ and $\tau_{\Omega} = \frac{1}{\Omega}$ determines the length of the ballistic regime. In Figure 4, the solutions for the MSD are presented for both the ABP and the chiral ABP, and the different regimes are clearly visible. Significant progress has been made in describing the behavior of micron scale chiral active particles inhomogeneous environments. Besides the chiral ABP, various models have been developed, many relying on stochastic descriptions [11–14]. For in homogeneous environments, that contain e.g. obstacles or boundaries, the interactions between the particle and its environment complicate the description, and it is often not possible to solve the equations of motion analytically. To study chiral active particles in such environments, we will have to resort to numerical methods, as will be explained below.

Numerical model of an ABP

The dynamics of an ABP in a heterogeneous environment is an example of the type of problem encountered in (active matter) physics, for which no or limited analytical solutions exist. In such cases, computational models or computer simulations can provide unique insights in the nature of the problem. The results of computer simulations are compared to experimental results to verify that the model represents well reality. If the model is found to be realistic, it can be used to assist experimentalists in interpreting results, and to explore systems that are more difficult to realise experimentally. An important benefit of computer simulations is that microscopic details of a system, such as particle size, mass, propagation speed and the interaction between particles, are often parameters of a model that can be separately controlled and independently studied [15, 16].

Simulations of active matter systems can be divided into different categories [17]. The first category consists of numerical implementations of "dry" models, in the case of the ABP model, simply called Brownian dynamics simulations. Due to their relative simplicity, Brownian dynamics simulations are intuitive to use and can be scaled to large numbers (10^7) of particles. Another very well known "dry" model is the Vicsek model, which includes alignment interactions between different particles and is often used to study flocking behavior. A second category consist of numerical implementations of "wet" to models which rely on solving the Navier-Stokes equation of the particle-solvent interaction numerically. For simple systems, this can be done directly by means of computational fluid dynamics, for more complex systems alternative approaches such as the Lattice Boltzman method exist.

To simulate the behaviour of a chiral ABP navigating a heterogeneous environment, the interaction with the environment needs to be included in the model, and the equations of motion (Eqs. 5 and 6) need to be discretized. For simplicity we will now consider a two dimensional environment soley containing repulsive, spherical obstacles. An efficient and numerically stable way to discretize the equations of motion is the second order Runge-Kutta integration scheme [18]. Interactions between the particle and the obstacles can be modeled with a repulsive force $\vec{F} = -\nabla V$, defined by the Weeks-Chandler-Anderson potential

$$V(r_{ij}) = \begin{cases} 4\epsilon \left[\left(\frac{\sigma}{r_{ij}}\right)^6 - \left(\frac{\sigma}{r_{ij}}\right)^{12} \right] & \text{for: } r_{ij} < 2^{\frac{1}{6}}\sigma, \\ 0 & \text{for: } r_{ij} \geq 2^{\frac{1}{6}}\sigma, \end{cases} \tag{12}$$

with ϵ denoting the potential well depth, σ the distance at which the potential is zero, and r_{ij} the distance between Active Brownian Particle i and obstacle j [16]. The discretized equations of motion are as follows

$$\begin{cases} x_i^{'}(t) = x_i(t) + F_{x,i}(r_i(t))\dfrac{\Delta t}{\gamma} + v\cos(\theta_i(t))\Delta t + \sqrt{2D_{\mathrm{T}}\Delta t}\, W_{x,i}, \\ y_i^{'}(t) = y_i(t) + F_{y,i}(r_i(t))\dfrac{\Delta t}{\gamma} + v\sin(\theta_i(t))\Delta t + \sqrt{2D_{\mathrm{T}}\Delta t}\, W_{y,i}, \\ x_i(t+\Delta t) = x_i(t) + \left[F_{x,i}(r_i(t)) + F_{x,i}(r_i^{'}(t))\right]\dfrac{\Delta t}{2\gamma} + v\cos(\theta_i(t))\Delta t + \sqrt{2D_{\mathrm{T}}\Delta t}\, W_{x,i}, \\ y_i(t+\Delta t) = y_i(t) + \left[F_{y,i}(r_i(t)) + F_{y,i}(r_i^{'}(t))\right]\dfrac{\Delta t}{2\gamma} + v\sin(\theta_i(t))\Delta t + \sqrt{2D_{\mathrm{T}}\Delta t}\, W_{y,i}, \\ \theta_i(t+\Delta t) = \theta_i(t) + \Omega_i\Delta t + \sqrt{2D_{\mathrm{R}}\Delta t}\, W_{\theta,i}, \end{cases} \tag{13}$$

where for particle i: $r_i(t) = (x_i(t); y_i(t))$ denote the position of the particle, v and θ are its speed and direction, Ω denotes its angular velocity ($\Omega = 0$ for a non-chiral ABP) and $F_i(r_i(t))$ denotes the force. $W_{x,i}$, $W_{y,i}$ and $W_{\theta,i}$ represent independent white noise stochastic processes with zero mean. The position of the particle $r_i(t)$ is updated in two steps. In the first step an intermediate position of the particle $r_i^{'}(t) = (x_i^{'}(t); y_i^{'}(t))$ is calculated by integrating the trajectory using $\vec{F}_i(r_i(t))$. The new position $r_i(t + \Delta t) = (x_i(t + \Delta t); y_i(t + \Delta t))$ is then calculated using $\vec{F}_i(r_i^{'}(t))$. The orientation $\theta_i(t)$ of the particle is updated in a single step using an Euler integration algorithm [9]. Now that we have discussed how to simulate the motion of an ABP, we can continue by addressing the ABP in an environment that contains obstacles.

Chapter 1

The role of disorder in the motion of chiral active particles in the presence of obstacles

Biological and man-made chiral active particles, rarely move in homogeneous environments, but rather encounter heterogeneity, in the form of boundaries (typically much larger than the particle) such as domain walls or pores, and smaller obtrusions or obstacles (typically of the size of the particle, or smaller) [8]. To address this, recent research efforts have been directed at understanding the underlying (bio)physical mechanisms of chiral active particles in heterogeneous environments [19]. From a fundamental perspective, this is interesting to understand and optimise search strategies in realistic environments [20, 21]. From a practical perspective, such an understanding is crucial to explain and control biomedically relevant processes, such as bio-film formation. In addition, there remains significant yet unexploited potential to enable novel nanotechnological applications, including smart self-propelled cargo carriers with uses in drug-delivery in tissue or contamination removal in porous soil, among others [22–26].

A first approach to control the dynamics of active particles in heterogeneous environments relies on designing the topography of the environment by carefully placing obstacles or structures on a surface. Another approach would be to design an active particle that is able to navigate a complex environment in a controlled manner [27]. This requires control over the reorientation of the particle, which has to date been achieved only in a limited number of cases [28, 29].

Experimental observations show that the topography of the environment can strongly influence the dynamics of microswimmers on a surface, in non-intuitive ways. Experimental evidence indicates that the presence of porous micro-structures generally hinders the diffusive transport of microswimmers [30, 31]. Interestingly, for chiral microswimmers, contrasting phe-

nomenology has also been observed. For example, a significantly enhanced propagation on surfaces, due to randomly placed obstacles, has been reported in theoretical studies [32–34] and in experiments with *E. coli* [35]. Furthermore, experiments tracking *E. coli* navigating a colloidal crystal revealed that the colloids rectify the trajectories of the bacteria, resulting in enhanced transport [36–39].

A common feature of natural and man-made heterogeneous environments is the presence of disorder or noise in the surface topography. Disorder can occur in the form of spatial positioning and size of obstacles or pores. Also the motion of active particles contains disorder in the reorientation, typically in the form of flagellar noise or rotational Brownian diffusion [28, 29, 40, 41].

The simplest interaction between chiral active particles and obstacles is a purely repulsive interaction. In this chapter, we examine numerically the effect of disorder (from here on referred to as 'noise') in the steric interactions on the dynamics of chiral active particles exploring a periodic arrangement of obstacles, where we introduce noise in a controlled manner. We first consider a chiral active particle that does not experience any rotational Brownian diffusion in a periodic array of obstacles. Distinct types of noise are then introduced independently: 'dynamic noise' determining the reorientation of the particle and two types of 'quenched noise', the first being disorder in the positions of the obstacles, and the second being polydispersity in the sizes of the obstacles.

To quantify the effect of the different types of noise on the transport properties of the active particle, we computed its effective diffusion coefficient (diffusivity) for a wide range of obstacle area fractions (densities) and noise strengths. We find that the diffusivity of a chiral active particle is strongly non-monotonic for increasing density of obstacles. At lower densities, the transport of a chiral active particle is rectified due to the interaction of the particle with the obstacles, affecting the orbits, and allowing the particle to explore space. At higher densities, the particle is unable to perform chiral motion due to constant interactions with the obstacles and the diffusivity is reduced until the conditions are right for the motion to be channeled in the lattice. When the strength of dynamic noise is increased, the diffusivity is enhanced for all but high densities, which we attribute to the randomization of the chiral orbits. Moreover, the ability of the particle to better explore space becomes less dependent on the obstacles. At high densities, dynamic noise suppresses guided transport through channels. Quenched noise introduces disorder in the spatial arrangement of the obstacles, resulting in erratic motion,

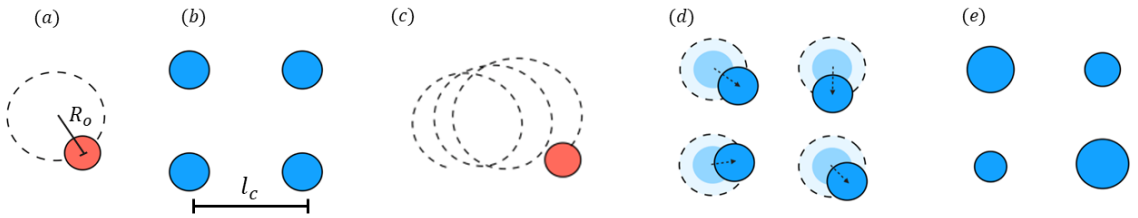

Figure 1.1: (a) Schematic depiction of an 'ideal chiral active particle' and its trajectory with orbit radius R_{o}. (b) Schematic depiction of four obstacles in a square lattice with lattice periodicity l_{c}. (c) Schematic depiction of the trajectory of a chiral active particle with low dynamic noise. (d) Lattice with quenched noise in the form of randomly perturbed obstacle positions. The arrows denote the change in position of the obstacles (dark blue circles) due to the positional quenched noise, relative to their original lattice position marked by the immediately lighter shade of blue. The lightest shade of blue marks the area from which a new position was chosen randomly. (e) Lattice with quenched noise in the form of obstacle polydispersity.

preempting fixed orbits, and perturbing guided motion through channels.

1.1 Model

We consider a spherically shaped chiral active particle of diameter σ (for *E. coli* typically 1-2 μm) on a surface containing N_{obstacle} fixed obstacles of equal diameter $\sigma_{\mathrm{obstacle}} = \sigma$. The amount of obstacles is expressed as the percentage of the surface that is covered by the obstacles: $\rho = \frac{\mathrm{N_{obstacle}}\pi\sigma^2}{L^2}$ ($\times 100\%$), with L being the edge size of the square simulation box. Interactions between the particle and the obstacles are defined by the Weeks-Chandler-Anderson potential $\mathbf{F} = -\nabla V$.

The initial position of the particle is randomly chosen in the box while guaranteeing that it does not overlap with any obstacle. The trajectory of the particle is then obtained by integrating the following equations:

$$\begin{cases} \dot{x} = v\cos(\theta) + F_x, \\ \dot{y} = v\sin(\theta) + F_y, \\ \dot{\theta} = \Omega + \sqrt{2D_{\mathrm{R}}}\,\xi_\theta, \end{cases} \tag{1.1}$$

where x, y denote the position of the particle, v and θ are its speed and direction, and F_x and F_y are the x and y components of the force. The angular velocity Ω results in periodic orbiting motion of the particle that is counterclockwise for $\Omega > 0$ and D_{R} defines the rotational diffusion constant. The stochastic term ξ_θ represents independent white noise with zero mean and unitary variance. The model reproduced well the experimental data for *E. coli* in [35]. The time evolution of the position of the particle is obtained with a second order Runge-Kutta scheme, to guarantee stability at high obstacle densities. As a reference particle, we consider an 'ideal

chiral active particle' with $v = 3\sigma$ and $\Omega = 1$, representing a chiral active particle that moves in perfect circles of radius $R_o = v/\Omega = 3\sigma$ when moving in a homogeneous environment (no obstacles and $D_R = 0$) as in Fig. 1.1 (a). As reference surface topography, we consider obstacles placed in a square lattice arrangement (Fig. 1.1 b).

Two types of noise are then introduced independently: dynamic noise in the dynamics of the particle ($D_R \neq 0$) (Fig. 1.1 c) and quenched noise either in the positions of the obstacles (Fig. 1.1 d) or in the form of obstacle size polydispersity (Fig. 1.1 e). For positional quenched noise, the strength is set by ξ_q, which defines the radius of a circular disk centered at the position of the obstacle; the perturbed obstacles are placed at a new random position chosen uniformly in this disk. For the obstacle size polydispersity, the size distribution follows a Gaussian with mean σ, and dispersion σ_s. For each obstacle, the diameter d is drawn from the size distribution, if $d \leq 0$ a new diameter is drawn from the distribution until a diameter $d > 0$ is obtained.

In this theis the effects due to inertia are neglected. However, recent studies indicate that for macroscopic active particles, inertial effects become increasingly relevant and require careful consideration [42–44].

In the following we will express distances in terms of the dimensionless obstacle radius $\sigma/2$ and time in terms of σ/v. A simulation typically includes $N_{\text{obstacle}} = 400$ obstacles. Finally, the step size in the simulation is $\Delta t = 10^{-4}$ and a simulation lasts for t = 4800 σ/v.

1.2 Results

To characterize the transport properties of the chiral active particle, we computed the mean square displacement:

$$\text{MSD}(t) = \left\langle [R(t) - R(0)]^2 \right\rangle, \tag{1.2}$$

with $R(t)$ denoting the position of the particle at time t. The brackets $\langle . \rangle$ indicate an ensemble average over 4000 particle trajectories, each beginning at a position selected uniformly at random. For positional quenched noise or size polydispersity, the average is performed over 100 obstacle configurations, with 40 particle trajectories per configuration. As discussed in the introduction, at long times, the mean squared displacement is expected to scale with the effective diffusion constant D or diffusivity,

$$\text{MSD}(t) \sim 4Dt, \quad t \to \infty. \tag{1.3}$$

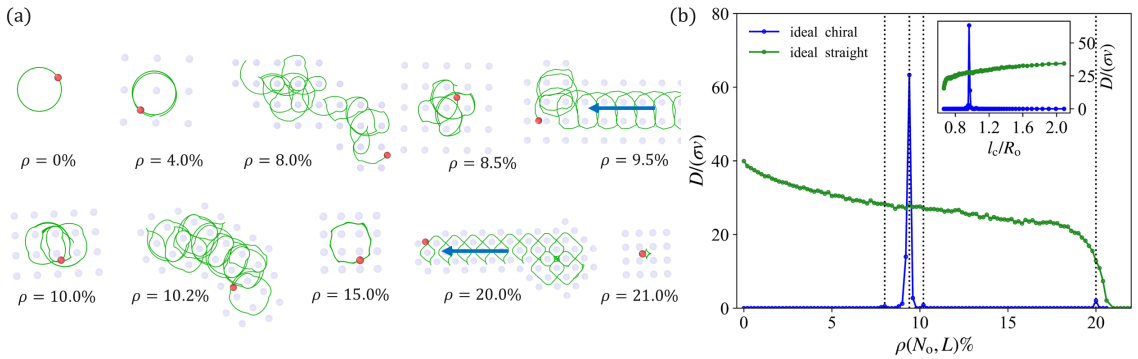

Figure 1.2: (a) Example trajectories (green) of the active particle (red) navigating the square lattice of obstacles (faint blue) for increasing densities. The blue arrows indicate the direction of propagation of the 'translating orbits'. (b) Diffusivity D vs. density of obstacles ρ for the 'ideal chiral active particle' and the 'ideal straight moving particle', which has been rescaled such that for $\rho = 0$, $D = 40.0$. The inset displays the diffusivity vs. the lattice periodicity l_c normalized by the orbit radius R_o. The dashed lines mark the densities for which diffusion occurs for the 'ideal chiral active particle'.

which we extracted through a linear regression in the interval $3600\sigma/v < t < 4800\sigma/v$. The diffusivity is measured for obstacle densities ranging from $\rho = 0\%$ representing a homogeneous environment (Fig. 1.2 (a) for $\rho = 0\%$) to $\rho = 21.0\%$, where the particle rapidly gets stuck in between obstacles (caged) and is unable to explore space (Fig. 1.2 (a) for $\rho = 21.0\%$).

1.2.1 Ideal chiral active particle

In the case of an 'ideal chiral active particle' ($D_R = 0$) in a homogeneous environment (without obstacles), the particle moves in a circular orbit of radius $R_o = 3\sigma$. More interesting behaviour emerges for a heterogeneous environment. A defining feature of the 'ideal chiral active particle' is that its space exploration is deterministic and a result of being scattered by the obstacles. The spatial distribution of obstacles alone governs its dynamics.

When an 'ideal chiral active particle' navigates a square lattice, the particle performs periodic orbits in between or around obstacles at most obstacle densities and is limited to exploring a small part of the system (or 'localized'), meaning that it does not perform long time diffusion. Example trajectories of 'localized' particles are presented in Fig. 1.2 (a) for $\rho = 0\%$, $\rho = 4.0\%$, $\rho = 8.5\%$, $\rho = 10.0\%$, $\rho = 15.0\%$ and a caged particle for $\rho = 21.0\%$. For a small number of intermediate densities the particle explores space, exhibiting long time 'diffusive' behaviour. Examples of diffusive behaviour are shown in Fig. 1.2 (a) for $\rho \approx 8.0\%$, $\rho \approx 9.5\%$, $\rho \approx 10.2\%$ and 20%. In Fig. 1.2 (b), the diffusivity D of the 'ideal chiral active particle' vs. ρ, is presented. The sharp peak in the diffusivity at $\rho = 9.5\%$ is a consequence of space exploration in the form of regular periodic motion. For densities around $\rho = 9.5\%$, the distance in between

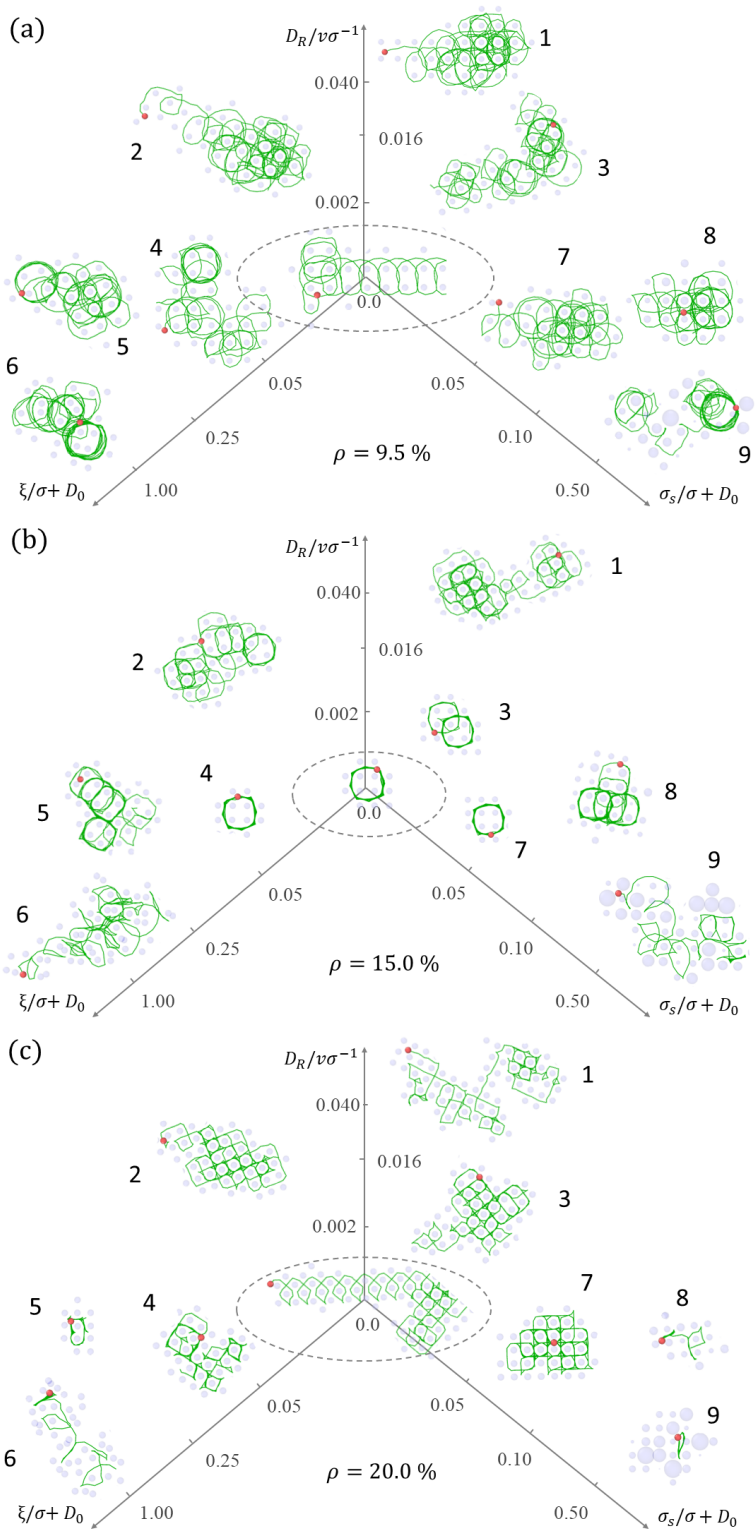

Figure 1.3: Example trajectories as a function of the different types of noise, for three increasing values of obstacle density: (a) $\rho = 9.5\%$, (b) $\rho = 15.0\%$ and (c) $\rho = 20.0\%$. The particle (red) traces a trajectory (green) moving among the obstacles (faint blue). In the middle, in the ellipsoid shape, the trajectory for the 'ideal chiral active particle' ($D_{\mathrm{R}} = 0$) in a square lattice, with no quenched noise, is shown as reference. The axes indicate the three different noise types: the vertical axis indicates the dynamic noise (D_{R}), the axis to the left the positional quenched noise (ξ) for a particle with $D_0 \equiv D_{\mathrm{R}}/v\sigma^{-1} = 0.002$, and the axis to the right quenched noise in the form of size polydispersity (σ_{s}).

neighbouring obstacles (the lattice periodicity, Fig. 1.1 b) l_c approximates the radius of the orbit R_o causing the particle to collide frequently with the surrounding obstacles. Around density $\rho = 9.5\%$, where $R_o \approx l_c$ (Fig. 1.2 b), the particle collides with an obstacle before it completes an orbit, and it is scattered forward towards the next row of obstacles. This 'translating orbit' (a term we borrow from skyrmions, where a similar effect was observed) is repeated for each row of obstacles, and results in the particle efficiently traversing the system. In Fig. 1.2 (a), an example trajectory is presented for $\rho = 9.5\%$. The blue arrow indicates the direction of propagation of the 'translating orbit'. At the two much smaller neighbouring peaks, for densities $\rho = 8.0\%$ (Fig. 1.2 a) and $\rho = 10.2\%$ (Fig. 1.2 a), the particle is scattered by the obstacles and traces mostly erratic trajectories with occasional laps of periodic behaviour. For higher densities, at $\rho = 20.0\%$, the particle is unable to trace chiral trajectories due to constant interactions with the closely spaced obstacles. Instead, it is guided through channels in the lattice, a trajectory traces a 'translating orbit' as the 'ideal chiral active particle' moves through the lattice (Fig. 1.2 a). Efficient transport in the form of 'translating orbits', resulting from a crowded topography, strongly contrasts with the behaviour of 'ideal straight moving particles' (particles with $D_R = 0$ and $\Omega = 0$), for which increasing the obstacle density monotonically hinders space exploration (Fig. 1.2 b).

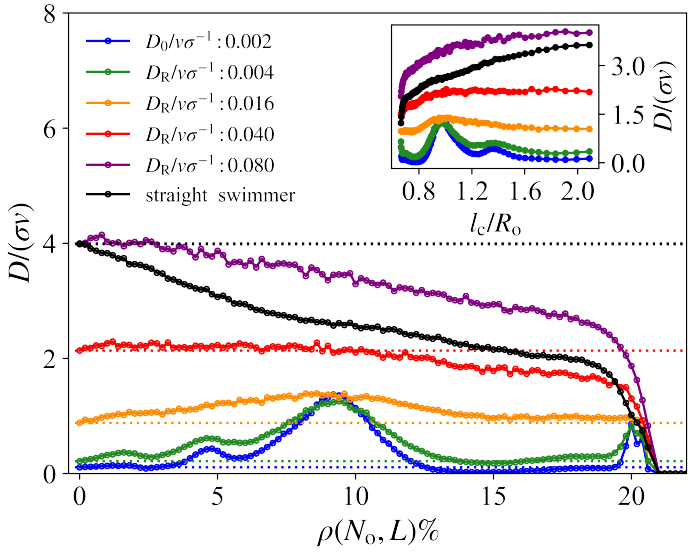

Figure 1.4: Diffusivity D vs. density of obstacles, for different dynamic noise amplitudes D_R. The inset displays the diffusivity vs. the lattice periodicity l_c for the obstacles, for a non perturbed lattice, normalized by the orbit radius R_o. The dashed lines indicate the diffusivity for a system without obstacles, and serve as a guide for the eye. The straight moving particle represents an active particle with with velocity $v = 3\sigma/s$, $\Omega = 0$ and D_0, and has been rescaled such that, for $\rho = 0$, it matches the curve with $D_R/v\sigma^{-1} = 0.080$.

1.2.2 Noise in the dynamics

When a chiral active particle exhibits noisy dynamics ($D_{\mathrm{R}} \neq 0$), the circular trajectory is perturbed allowing the particle to explore space. For a chiral active particle experiencing rotational diffusion with strength D_{R}, $\tau_{\mathrm{R}} = D_{\mathrm{R}}^{-1}$ sets the typical time for the particle to decorrelate from its initial direction of motion in free space.

Let us now consider a chiral active particle moving through a square lattice of obstacles. In Fig. 1.3 (a-c) some example particle trajectories are presented for different densities of obstacles. The noise in the dynamics is represented by the vertical axis ($D_{\mathrm{R}}/v\sigma^{-1}$). In Fig. 1.4 the diffusivity is presented for different noise amplitudes D_{R}. The dashed line indicates the diffusivity for the chiral active particle in a homogeneous environment (without obstacles); by comparing the diffusivity for a given noise strength to the homogeneous case $D(D_{\mathrm{R}}, \rho = 0)$, we can determine the effect of the obstacles on the diffusivity. When a diffusivity curve dips below the dashed line, the presence of obstacles hinders diffusion.

For the smallest noise strength ($D_0 \equiv D_{\mathrm{R}}/v\sigma^{-1} = 0.002$), the diffusivity profile is clearly non-monotonic with increasing obstacle density (Fig. 1.4). The noise perturbs the localized orbits of the 'ideal chiral active particle', resulting in diffusive behaviour for all densities $\rho < 20.5\%$. For higher densities, the particle is caged by the obstacles and the diffusivity vanishes. A fine structure with four peaks emerges, around densities $\rho = 2.0\%$, $\rho = 4.5\%$, $\rho = 9.5\%$ and $\rho = 20.0\%$. Less pronounced minima occur at $\rho = 2.5\%$, $\rho = 6.0\%$ and $\rho = 15.0\%$. For densities $\rho < 7.5\%$, the fine structure does not qualitatively change the behaviour of the particle, only resulting in a small enhancement or suppression of the diffusion. The fine structure is a result of the chiral active particle interacting with the periodic lattice, and disappears if the lattice is sufficiently perturbed, which will be explored in depth in paragraph 1.2.3.

To understand the main features of the diffusivity (Fig. 1.4), we can look at the number of orbits $n = \frac{\Omega}{2\pi D_{\mathrm{R}}}$ a particle typically completes (in a homogeneous environment) before its orientation is randomized by the dynamic noise, as suggested by [33]. For the small noise strength ($D_{\mathrm{R}}/v\sigma^{-1} = 0.002$), we obtain $n = 159$, implying that the particle still largely traces a circular trajectory if it does not interact with the obstacles. In this case, the increased diffusion can be attributed to efficient scattering by obstacles, rectifying the orbits, and enhancing the particle's diffusion. This mechanism dominates for intermediate densities, especially around $\rho = 9.5\%$ where the radius of the orbit R_{o} approximates the spacing between obstacles l_{c}, such that $l_{\mathrm{c}}/R_{\mathrm{o}} \approx 1$ (Fig. 1.4 inset). Some example trajectories are presented along the vertical axis

($D_{\mathrm{R}}/v\sigma^{-1}$) in Fig. 1.3 (a.1-3). The suppression of the diffusion for densities around $\rho = 15.0\%$ results from the particle becoming intermediately trapped in trajectories that orbit around a few obstacles. Due to the interactions with the obstacles, the particle keeps moving in a fixed orbit until, driven by dynamic noise, it hops (diffuses) to the next row of obstacles. Similar orbits were also observed for the 'ideal chiral active particle' for densities around $\rho = 15.0\%$, but since the 'ideal chiral active particle' does not experience dynamic noise, it remains trapped indefinitely (Fig. 1.2 for $\rho = 15\%$). In Fig 1.3 (b.3), an example trajectory is presented of a particle that hopped to a new orbit once. At higher densities the channels narrow further; now a small deviation in the trajectory more readily results in the particle hopping across rows, enhancing diffusion. Around density $\rho = 20.0\%$ (the highest densities before caging occurs), the frequent interactions with the closely spaced obstacles prevent the particle from moving in circular orbits. Instead, the particle is guided through channels in the lattice, in an erratic way, efficiently exploring space. In Fig. 1.3 (c.1-3) some example trajectories of a particle with dynamic noise navigating a dense system with $\rho = 20.0\%$ are presented. For higher densities $\rho \geq 20.5\%$, the particle is fully caged in the lattice.

Now that the general behaviour of a noisy chiral active particle is outlined, we can examine the effect of increasing the noise strength D_{R} (Fig. 1.4). As a reference, we take the previous case of a particle with $D_{\mathrm{R}} = D_0$. For a small increase in the noise strength to $D_{\mathrm{R}}/v\sigma^{-1} = 0.004$, and $n = 80$, the behaviour is similar to the reference case. When the noise is increased to $D_{\mathrm{R}}/v\sigma^{-1} = 0.016$, we obtain $n = 20$; now the presence of obstacles enhances the diffusivity for all densities in a more uniform manner, but still peaks around $\rho = 9.5\%$, before flattening out. Limited enhancement is observed for densities $\rho > 15\%$ until it vanishes for $\rho \geq 20.5\%$. In this case, the noise is too strong for the particle to remain trapped in fixed periodic orbits for an extended period of time. Instead, the particle moves across the lattice in an erratic way, along with intermittent periods of orbiting around (multiple) obstacles (Fig. 1.3 (a-c.2)). The diffusion of such erratic motion is not very sensitive to the density; the diffusivity varies little for $\rho > 15.0\%$, until it vanishes at $\rho = 20.5\%$ as the particle becomes caged by the obstacles.

For still larger noise strengths ($D_{\mathrm{R}}/v\sigma^{-1} = 0.040$ and $D_{\mathrm{R}}/v\sigma^{-1} = 0.080$), the noise increasingly perturbs the orbiting motion, the particle's motion is markedly less chiral, typically only able to perform $n = 8$ orbits ($D_{\mathrm{R}}/v\sigma^{-1} = 0.040$) and $n = 4$ orbits ($D_{\mathrm{R}}/v\sigma^{-1} = 0.080$) before its orientation is fully decorrelated. In this case, the particle traces strongly erratic trajectories for all densities, which are not very sensitive to the density. Some example trajectories are pre-

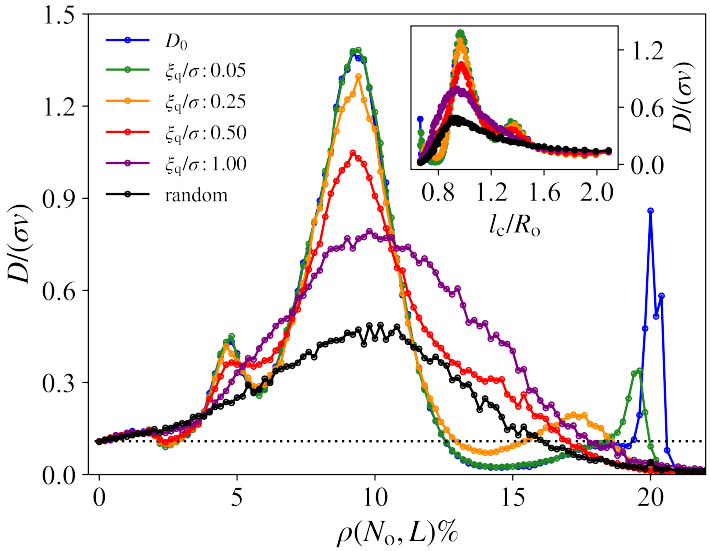

Figure 1.5: Diffusivity D vs. density of obstacles, with $D_R/v\sigma^{-1} = D_0 = 0.002$ for different lattice perturbation amplitudes ξ_q. The inset displays the diffusivity vs. the lattice periodicity l_c for the obstacles, for a non perturbed lattice, normalized by the orbit radius R_o. The dashed lines indicate the diffusivity for a system without obstacles, and serve as a guide for the eye. The random system represents a regular chiral active particle with D_0, in a system with randomly placed non overlapping obstacles.

sented in Fig. 1.3 (a-c.1) for $D_R/v\sigma^{-1} = 0.040$. Scattering by obstacles enhances diffusion only marginally for low densities $\rho < 9.5\%$ ($D_R/v\sigma^{-1} = 0.040$) and $\rho < 3.0\%$ ($D_R/v\sigma^{-1} = 0.080$). Moreover, the diffusivity varies little with the density for $\rho < 9.5\%$ ($D_R/v\sigma^{-1} = 0.040$) and $\rho < 3.0\%$ ($D_R/v\sigma^{-1} = 0.080$). For higher densities, similarly to the 'straight moving particle' (black curve in Fig. 1.4), a monotonic decrease in diffusivity for increasing density is retrieved, vanishing for $\rho \geq 20.5\%$ where the particle is caged in the lattice.

1.2.3 Randomness in the positions of the obstacles

When a chiral active particle with D_0 explores a lattice with noise in the positions of the obstacles, the diffusivity is markedly affected for large strengths of noise. In Fig. 1.5, the diffusivity is presented for different amplitudes of the noise ξ_q, alongside the diffusivity of a configuration with randomly placed non-overlapping obstacles. The largest noise strength ($\xi_q/\sigma = 1.00$) corresponds to configurations where the contact between obstacles at density $\rho = 20.0\%$ is still low, with typically less than 10.0% of the obstacles touching. In Fig. 1.3, noise in the positions is represented on the left axis ($\xi/\sigma + D_0$).

For the smallest noise strength ($\xi_q/\sigma = 0.05$), at low densities ($\rho < 7.0\%$), the fine structure is little affected. The diffusivity profile is affected for high densities ($\rho > 17.0\%$), with the peak around $\rho = 20.0\%$ being significantly suppressed and shifted towards lower density values with

respect to the ordered lattice ($\xi_q/\sigma = 0$). The shift in the position of the peak around $\rho = 20.0\%$ is a result of the obstacles guiding the particle through (disordered) channels, leading to a small local maximum in the diffusivity for densities around $\rho = 19.5\%$. For higher densities, the randomness combined with the densely spaced obstacles perturbs the channels, and introduces significant backtracking of the trajectories, reducing the diffusivity when compared to the ordered lattice (Fig. 1.3 (c.4)). At the highest densities $\rho > 19.5\%$, the obstacles are closely spaced; even a small perturbation of the channels introduces bottlenecks impeding the particle to pass through, limiting diffusion.

When the noise is increased to $\xi_q/\sigma = 0.25$, the peak is shifted towards lower densities, channels are randomized further and bottlenecks occur at lower densities. Now, the disordered obstacles preempt the particle from getting trapped for long in intermittently stable orbits around a number of obstacles, as observed in the ordered lattice for densities around $\rho = 15.0\%$ (Fig. 1.3 (b.4) and for the 'ideal chiral active particle' 1.2 a). The particle is scattered randomly and diffuses more efficiently (Fig. 1.3 (b.5)), reducing the depth of the local minimum in the diffusivity. As the lattice perturbation is increased, bottlenecks occur at lower densities ($\rho > 18.0\%$). An example trajectory is presented in Fig. 1.3 (c.5).

For large amplitudes of positional noise ($\xi_q/\sigma = 0.50$ and $\xi_q/\sigma = 1.00$), with the average random displacement comparable to the obstacle size, the lattice is strongly perturbed. This results in a smoothing out of the fine structure of the diffusivity profile for all densities. In the limit of large positional quenched noise, a random topography is retrieved, and the diffusivity exhibits a single flattened peak, centered around $\rho = 10.0\%$ (black curve in Fig. 1.5). Due to the positional disorder, the distance between obstacles becomes irregular. This leads to suppression of the diffusion for densities around $\rho = 9.5\%$, as the disordered arrangement preempts regular motion where the particle moves from one row of obstacles to another, instead it is scattered randomly. As the lattice is further perturbed, this effect becomes increasingly pronounced (Fig. 1.3 (a.4-6)). Even for a fully random arrangement, the diffusion is enhanced for densities $\rho < 17.0\%$, indicating that for all but high densities of randomly placed obstacles, the rectification of orbits by obstacles leads to enhanced diffusion. For large amplitudes of positional noise (and the random configuration), and increasing densities $\rho > 17.0\%$, the strongly disordered and densely packed arrangements increasingly contain pockets of obstacles that trap the particle, limiting diffusion. A trajectory of a particle in a strongly disordered lattice that ultimately becomes trapped in a fixed orbit is displayed in Fig. 1.3 (c.6).

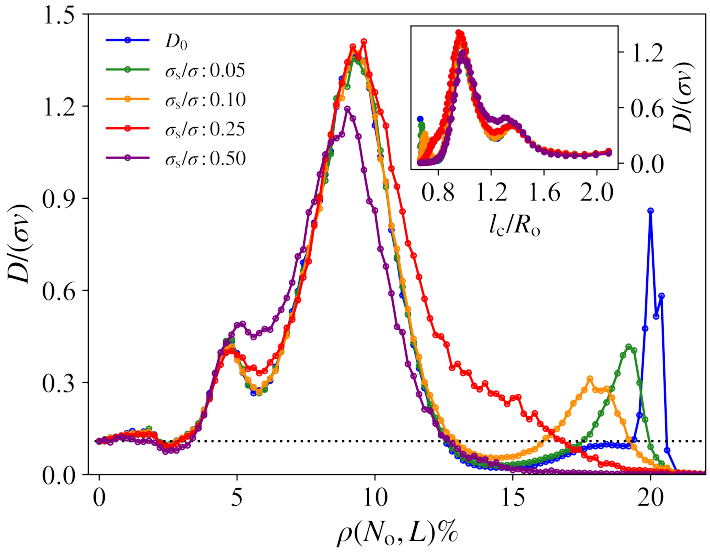

Figure 1.6: Diffusivity D vs. density of obstacles, with $D_R/v\sigma^{-1} = D_0 = 0.002$ for different amplitudes of size polydispersity σ_s. The inset displays the diffusivity vs. the lattice periodicity l_c for the obstacles, for a non perturbed lattice, normalized by the orbit radius R_o. The dashed lines indicate the diffusivity for a system without obstacles, and serve as a guide for the eye.

1.2.4 Non-uniform size distribution

For a non-uniform obstacle size distribution, σ_s sets the strength of the obstacle size polydispersity. In Fig. 1.6, the diffusivity is presented for different σ_s. Here the limit of large polydispersity ($\sigma_s/\sigma = 0.50$) corresponds to configurations with about 20.0% of obstacles, typically the largest, touching at density $\rho = 20.0\%$. The right axis in Fig. 1.3 represents the size polydispersity ($\sigma_s/\sigma + D_0$).

When navigating a surface with polydisperse obstacles, the diffusivity profile for a particle with D_0 is affected similarly to the system with positional quenched noise. For the smallest polydispersity ($\sigma_s/\sigma = 0.05$), at densities $\rho < 17.0\%$, the fine structure is little affected, as the particle traverses the system in an erratic way (Fig. 1.3(a.7) provides an example for $\rho = 9.5\%$). For higher densities $\rho > 17.0\%$, similar to the positional noise, the shift in the position of the peak around $\rho = 20.0\%$ is a result of the obstacles guiding the particle through channels of irregularly sized obstacles (similar to Fig. 1.3 (c.7)). This leads to a local maximum in the diffusivity for densities around $\rho = 19.0\%$. For still higher densities bottlenecks and pockets form that trap the particle. When the polydispersity is increased slightly to $\sigma_s/\sigma = 0.10$, the effect of intermittent trapping in orbits for densities around $\rho = 15.0\%$ is reduced (Fig. 1.3 (b.8)) and the peak is smeared out and shifted to lower densities.

For polydispersity $\sigma_s/\sigma = 0.25$, the fine structure is smoothed out for $\rho > 12.0\%$ as the

particle explores the system efficiently tracing erratic trajectories, until it increasingly becomes trapped for $\rho > 18.0\%$ and the diffusivity vanishes (Fig. 1.3 (c.8)). When the polydispersity is increased to $\sigma_s/\sigma = 0.50$, the fine structure is smoothed out for all densities, the peak around $\rho = 9.5\%$ is shifted to slightly lower densities and is reduced as the trajectories are randomized and periods of intermittent trapping in orbits occur (Fig. 1.3(a.9)). The shifting of the peak can be explained by the larger total surface covered by the obstacles due to the size polydispersity (what is gained by the obstacles that increase in size is not offset by what is lost by the obstacles that become smaller). For $\sigma_s/\sigma = 0.50$ the diffusivity is suppressed relatively to $\sigma_s/\sigma = 0.25$, for almost all densities. This is a result of some of the obstacles becoming increasingly larger; for $\rho > 8.0\%$ the large obstacles form clusters that trap the particle, as well as walls that subdivide the system and prevent the particle from accessing parts of it. For $\rho > 15.0\%$, the diffusivity vanishes rapidly as the particle becomes caged in pockets of obstacles. In Fig. 1.3(a-c.9), some example trajectories are displayed for noise amplitudes $\sigma_s/\sigma = 0.50$. When the polydispersity is further increased ($\sigma_s/\sigma > 0.50$), some obstacles become much larger than the particle; in this limit particle-obstacle interactions become more important, and our simplified model is no longer expected to accurately capture the dynamics [45, 46].

1.3 Discussion

In this chapter, we investigated the dynamics of a chiral active particle on a surface with obstacles. Different densities of obstacles as a fraction of the surface area were considered. We introduced distinct types of disorder: noise in the dynamics of the particle and noise in the positions of the obstacles, as well as obstacle size polydispersity.

A noiseless chiral active particle in an environment without obstacles gets trapped in circular orbits and does not explore space. When navigating an array of regularly spaced obstacles, for most densities, space exploration of a chiral active particle is limited to fixed orbits. Efficient long time transport, in the form of a 'translating orbit', occurs when the distance between the obstacles approximates the orbit radius of the particle, or the spacing between the obstacles approximates the size of the particle. Less efficient long time transport occurs for a few densities, with the particle tracing an erratic trajectory.

A chiral active particle that experiences dynamic noise performs long time transport for all densities, except for very high densities when it becomes trapped by the obstacles. The presence

of low to intermediate densities of obstacles enhances the transport of a chiral active particle, by rectifying orbits. Especially when the distance between the obstacles approximates the radius of the orbit, this effect is pronounced. For higher densities, obstacles can enhance transport by guiding the particle through open channels in the lattice.

When the strength of the dynamic noise is increased, the chiral trajectories are more strongly perturbed. This reduces the tendency of the particle to move in circles, enhancing transport for all densities, and reducing the effect of scattering by obstacles on the transport. For large noise amplitudes, the particle is effectively no longer chiral. In this case, the presence of obstacles hinders transport, which is in agreement with previously published results for non-chiral active particles [30, 31].

Positional noise and obstacle size polydispersity result in a disordered environment, which enhances transport by preempting fixed orbits in between or around obstacles. Additionally, scattering of the particle by the disordered obstacles results in erratic motion. For densities where the inter-obstacle distance approximates the radius of the particle's orbit, such motion perturbs the otherwise efficient rectification of orbits, and suppresses transport.

For high densities, quenched noise perturbs channels, limiting, and suppressing transport. For high densities and large quenched positional disorder or size polydispersity, pockets of obstacles form that trap the particle, strongly hindering transport. In the limit of large positional noise, the presence of a low or intermediate density of obstacles enhances transport. When the obstacle size polydispersity is increased, the dynamics is increasingly hindered by a few very large obstacles that form pockets that trap the particle, inhibiting long term transport. These findings are in line with a recent experimental and numerical study of (non chiral) active particles exploring a complex micro structure [47], where the authors found a coupling between the active force and the topography of the micro structure that strongly influences the effective diffusivity of the particles. In the future, this effect could be explored further for chiral active particles. In addition, differently shaped (non spherical) obstacles could be considered, and depending on the shape, these might promote the emergence of a preferred direction of motion or the trapping for the active particles.

We solely considered steric (repulsive) interactions. For wet active systems, as e.g. microswimmers, hydrodynamic interactions with the obstacles are also likely to affect the dynamics. For example, in [35] it has been shown that for *E. coli*, hydrodynamic interactions with obstacles (forward scattering) are the key mechanism responsible for an enhancement in the

diffusion for an optimal density of random obstacles. Here, we show that in the absence of hydrodynamic interactions, diffusion of a chiral active particle is also enhanced, although through a different physical mechanism. Future works might include the role of hydrodynamic effects in the particle-obstacle interaction, such effects can introduce an attractive interaction that deflects the particle in the absence of a particle-obstacle collision [45, 46]. Moreover, in the case of a strong attraction, the particle might get trapped by the obstacles due to the attraction alone, potentially introducing new localized states.

An interesting extension of this work would be to investigate the effect of spatial arrangement and disorder on the dynamics of interacting chiral active particles. Previous work encountered motility induced phase separation, commensuration effects and frustrated states for a simple model of interacting non-chiral particles in a similar square lattice of obstacles [48]. Another possibility would be to consider moving obstacles. The bronchus in the lungs are lined with respiratory cilia: microscopic, periodically beating hairs that clear inhaled debris and microbes from the conducting airways [49]. By introducing a periodic motion in the obstacles, the dynamics governing the transport of (chiral) microbes in the cilia could be explored. From a very different perspective, simulation studies of circular ac driven skyrmions on a square lattice of obstacles encountered behaviours similar to our findings for the 'ideal chiral active particle' [50]. It could be interesting to see how such systems respond to noise. Although this work is limited to surface topography, extending it to three dimensions would also be interesting, as will be discussed in the next chapter. Recently a geometric criterion for the optimal transport of run and tumble polymers in a porous medium was uncovered, which emerges when their run lengths are comparable to the longest straight path available in the porous medium [39]. In addition to a fundamental understanding of the dynamics of chiral active particles in complex environments, these findings can be employed to guide the future design of active searchers capable of optimal navigation in complex environments, or the development of micro-structured surfaces that can control and prevent bacterial adhesion.

This chapter followed closely: D. M. van Roon, G. Volpe, M. M. Telo da Gama, and N. A. M. Araújo, "The role of disorder in the motion of chiral active particles in the presence of obstacles," Soft Matter, vol. 18, pp. 6899–6906, 2022.

Chapter 2

3D model for the surface accumulation of chiral and non-chiral microswimmers

An important property of active matter is the inherent asymmetry in the interaction of active particles with boundaries. When approaching a boundary, an active particle will swim along (or against) it, effectively becoming 'trapped' at the boundary, until its direction of motion is pointed away from it. When moving away from a boundary, the particle will move freely, until it encounters another boundary. Due to this asymmetry, active particles tend to accumulate near boundaries, even when they are purely repulsive [8, 19, 51, 52]. For passive particles such accumulation near boundaries is not observed, and would require an attractive interaction. Steric effects and the persistence in the swimming direction are generic contributing factors to surface accumulation, in addition to hydrodynamic effects that depend on the specifics of the swimmer and the surface. For example, they may result in stable swimming trajectories following the boundary, even if the boundary is convex [45, 46, 53]. Furthermore, driven by hydrodynamic interactions, several microswimmers move in chiral trajectories, typically along circles, when swimming near a flat interface [4–7].

Bacterial surface dynamics are central in various industrial, biomedical, and environmental processes [21, 54, 55]. On the one hand, the adhesion of bacteria to surfaces frequently results in the formation of persistent biofilms that are difficult to remove, causing challenges in various fields, including fouling of water purification systems [56], corrosion of structures used to transport and store chemicals [57], and adhesion to medical implants, where bacterial infection can result in inflammation that can even lead to death [58]. On the other hand, the industrial potential of biofilms is becoming increasingly developed, including biorefineries [59], bioreme-

diation to remove contaminants from freshwater and wastewater [60], and as templates for new materials with applications in construction and industry [61].

A quantitative understanding of surface entrapment and subsequent adhesion could further the development of engineered materials to control and prevent bacterial adhesion to surfaces [62–64]. In recent years, the effects of surface topography and roughness on bacterial surface dynamics and adhesion have received increasing attention. Recent experiments on *E. coli* approaching a surface, have shown that the average reorientation of the cells in a direction parallel to the surface is driven by steric forces at contact and short-ranged hydrodynamics, with long-range hydrodynamics playing only a minor role [65–68]. Similar results were obtained for sperm cells on a surface [69], for *E. coli* interacting with microsized pillars [53] and for synthetic microswimmers navigating an environment of passive colloidal beads [45]. After the reorientation event, a swimmer was observed to move along a boundary (surface, pillar or bead) until Brownian diffusion rotates its axis away.

In this chapter we introduce a 3D model to examine the surface accumulation of microswimmers induced by steric forces and an effective short-ranged hydrodynamic alignment force that aligns the propagation direction of the swimmers along the nearest boundary. We take *E. coli* and bull sperm cells as examples, navigating a volume bounded by a top surface plane and a bottom one, akin to a microfluidic channel. We study the effect of placing convex obstacles, which are three times the size of the swimmers, randomly on both surfaces. We examine how the surface accumulation is impacted by the strength of the alignment force and the angular velocity of the motion. We quantify the surface accumulation by measuring the fraction of swimmers near the surfaces. We find that the presence of obstacles always reduces the accumulation of non-chiral microswimmers on these surfaces, as, by aligning along the boundary of the obstacles, the swimmers are directed away from the surface. As the obstacle density is increased, the surface accumulation is reduced. For chiral microswimmers, the accumulation can be reduced or enhanced. As previously observed in [45, 46, 53], we confirm with our model that a chiral swimmer may get trapped. This orbital trapping results from an interplay of the alignment force with the chiral motion of the swimmer, and only occurs if the obstacles are at least equal to the size of the swimming orbit. We discuss how obstacles can be used to control the accumulation of chiral swimmers near surfaces, by carefully tuning their size. In addition, we discuss how obstacles can be employed to sort swimmers based on their angular velocity.

2.1 Model

We consider a spherically shaped swimmer of diameter σ (for natural and synthetic microswimmers typically 1-5 μm) moving with velocity $\vec{v}$ and corresponding momentum $\vec{p}$. The swimmer navigates a volume of thickness 100σ bounded by a top and bottom square surface plane, with edge size L and periodic boundary conditions along the directions parallel to the surfaces. Each surface plane is covered with N_{obstacle} non-overlapping obstacles of diameter $\sigma_{\text{obstacle}} = 6\sigma$, distributed uniformly at random. The obstacles are quantified by the surface coverage defined as: $\rho = \frac{\text{N}_{\text{obstacle}}\pi{\sigma_{\text{obstacle}}}^2}{4L^2}$ ($\times 100\%$). The motion of the swimmer is determined by the force acting on it, and a stochastic term $\vec{\xi}$ that is parameterized to set a proper rotational diffusion constant for the swimmer. The force has two contributions: $\vec{F}_{\text{motile}}$ responsible for the self-propelled motion in the volume and $\vec{F}_{\text{surface}}$ describing the interaction with the surface. The trajectory of the swimmer is obtained by integrating the following equation

$$\dot{\vec{p}} = \vec{F}_{\text{motile}} + \vec{F}_{\text{surface}} + \vec{\xi}. \tag{2.1}$$

The motile force is

$$\vec{F}_{\text{motile}} = -\frac{1}{\tau}(\vec{p} - p_0\hat{p}), \tag{2.2}$$

which drives the motion along a predefined direction $\hat{p}$, with a momentum of magnitude p_0. The timescale of the motility is set by τ. For the surface interaction we take

$$\vec{F}_{\text{surface}} = -\alpha(\hat{p}\cdot\hat{\mu}_\perp)\hat{\mu}_\perp + \beta(\hat{p}\times\hat{\mu}_\perp) + \vec{F}_{\text{steric}}, \tag{2.3}$$

where the first term is an effective alignment force between the swimmer and an obstacle or surface plane, the second term is the angular velocity of the motion when the swimmer approaches the surface, and the last term is the steric interaction of the swimmer with the obstacles and the surface. The strength of the alignment interaction is determined by α. For $\alpha > 0$ the force will align the swimmer along the obstacle boundary or surface plane, with $\hat{\mu}_\perp$ the unit vector perpendicular to the obstacle boundary or surface plane closest to the swimmer [65, 66].

For $\beta > 0$, the swimmer will trace circular trajectories when moving close to the surface. The orbital radius of the trajectories R_{o} is determined by β and defined as $R_{\text{o}} = \frac{v}{\beta}$. We introduce $\Omega = \frac{\sigma_{\text{obstacle}}}{2R_{\text{obstacle}}}$ as a measure of the angular velocity, by normalizing the size of the obstacles with the size of the swimming orbit. For larger values of β swimmers trace smaller orbits

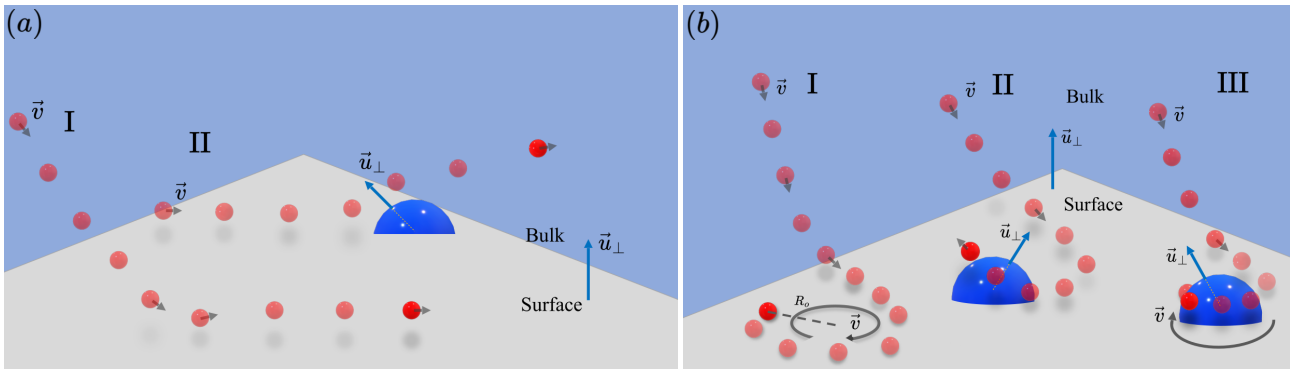

Figure 2.1: (a,b) Schematic depiction of a swimmer (red) moving at velocity $\vec{v}$ in the volume (blue) near the surface (light grey). The dark grey arrows indicate the direction of motion of the swimmer, the blue arrows indicate the vector perpendicular to the closest surface plane, or the boundary of the closest obstacle (dark blue hemisphere). (a) A non-chiral swimmer (I) approaching the surface, (II) guided away from the surface after interacting with the obstacle. (b) A chiral swimmer ($\Omega \neq 0$) (I) approaching the surface, where it moves in orbits of radius R_o, (II) guided away from the surface after interacting with the obstacle, (III) trapped in an orbit around the boundary of the obstacle.

corresponding to larger values of Ω. Experimentally, Ω could be controlled through the obstacle size, with larger obstacles resulting in larger Ω [53, 70]. A schematic illustration of a non-chiral swimmer ($\beta = 0$) is shown in Fig. 2.1 (a,I), and an illustration of a chiral swimmer in Fig. 2.1 (b,I). To represent the short-ranged nature of the interactions, a cut-off distance $r_c = \frac{3\sigma}{2}$ is introduced, such that, when the distance r between swimmer and the obstacle boundary or surface plane is $r > r_c$, α and β are set to 0.

The last term in eq. 2.3 is the steric interaction. A truncated Weeks-Chandler-Anderson potential is used to represent the steric interaction with the obstacles as it is a well tried method for including obstacle-swimmer interactions [34, 35]. For the surface we use an exponential repulsion of magnitude

$$F_{\text{surface}} = \frac{1}{r_s} \exp\left(-r_s\right), \tag{2.4}$$

with r_s the distance between swimmer and surface. The interaction becomes effective when $r_s < \frac{\sigma}{2}$. The time evolution is obtained by integrating the system with the velocity Verlet method. In the following we will express distances in terms of the dimensionless swimmer radius $\sigma/2$ and time in terms of σ/v. A simulation typically includes $N_{\text{obstacle}} = 100$ obstacles on each surface plane, for a total of 200 obstacles. Finally, the step size in the simulation is $\Delta t = 10^{-4}$, $\tau = 1$ and a simulation lasts for t = 3600 σ/v.

2.2 Results

To characterize the surface accumulation, we count the number of swimmers N_{surface} that are at a distance shorter than 3σ (one obstacle radius) from the bottom or top surfaces in the steady state of the system. We define the fraction ϕ of microswimmers accumulated at the surfaces as,

$$\phi = \langle \frac{N_{\text{surface}}}{N} \rangle. \tag{2.5}$$

The brackets $\langle . \rangle$ indicate an ensemble average over $N = 25000$ swimmer trajectories (the swimmers do not interact), each beginning at a position selected uniformly at random within the volume. For smooth surfaces $\rho = 0$, the surface planes contain no obstacles. For surfaces with obstacles, each surface plane is covered with N_{obstacle} non-overlapping hemispherical obstacles, uniformly and randomly placed on the surface, such that their centres are on the surface plane. Results of 250 swimmer trajectories are averaged over 100 obstacle configurations, for a total $N = 25000$ swimmer trajectories. Two different values for the rotational diffusion will be considered, $D_{\text{R}} = 0.1\ \text{rad}^2/\text{s}$ corresponding to the rotational diffusion measured for *E. coli* [67], and $D_{\text{R}} = 10^{-4}\ \text{rad}^2/\text{s}$ corresponding to the value for bull sperm [69].

2.2.1 Smooth surface

To set the stage first consider the simplest case of non-chiral ($\Omega = 0$) swimmers navigating a volume bounded by smooth surfaces, where the surface accumulation ϕ increases with the alignment force strength α. Fig. 2.2 (a,b) (blue diamonds) shows how the surface accumulation ϕ increases with α ranging from $\alpha = 0$, where the rotational diffusion governs the dynamics, to $\alpha = 60$, where the alignment force dominates.

In the absence of alignment force ($\alpha = 0$), about 15% ($D_{\text{R}} = 10^{-4}\ \text{rad}^2/\text{s}$, Fig. 2.2 a) and 12% ($D_{\text{R}} = 0.1\ \text{rad}^2/\text{s}$ Fig. 2.2 b), swimmers accumulate near the surface. This accumulation is a result of the persistent motion of the swimmers. A swimmer explores the volume until it collides with one of the surfaces, where it will stay until rotational diffusion directs it away from it, and it can escape.

As the alignment force increases, the fraction of swimmers accumulated near the surfaces increases. This behaviour can be explained by considering that the alignment force competes with the rotational diffusion, as a stronger tendency to align prevents the swimmer from orienting away from the surface and escape. The marked increase in accumulation for $0 < \alpha < 10$

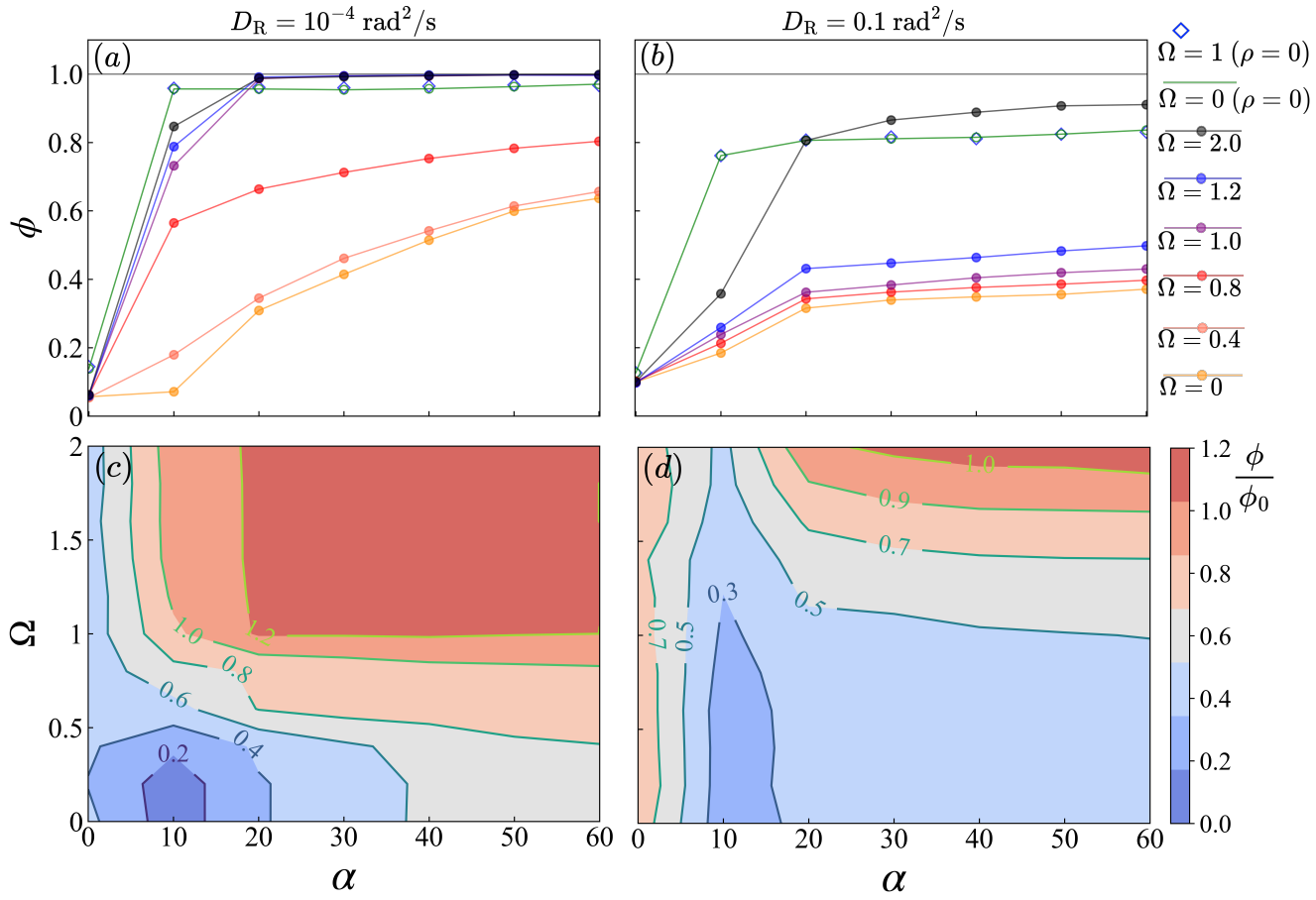

Figure 2.2: (a,b) Fraction of swimmers accumulated on the surface ϕ against the alignment force α for different angular velocities Ω, with an obstacle surface coverage $\rho = 20\%$: (a) for swimmers with $D_R = 10^{-4}$ rad^2/s and (b) for swimmers with $D_R = 0.1$ rad^2/s. (c,d) Fraction $\frac{\phi}{\phi_0}$ of swimmers accumulated on a surface with convex obstacles relative to the fraction accumulated at a smooth surface ϕ_0, as a function of Ω and α, (c) for $D_R = 10^{-4}$ rad^2/s and (d) for $D_R = 0.1$ rad^2/s.

results from this competition. For $D_{\mathrm{R}} = 10^{-4}\ \mathrm{rad}^2/\mathrm{s}$ (Fig. 2.2 a) when $\alpha \geq 10$ the alignment force becomes strong enough to trap the swimmer at the surface. The trapping results in an enhanced accumulation, which increases with the alignment force, reaching 95% for $\alpha \geq 10$. When $D_{\mathrm{R}} = 0.1\ \mathrm{rad}^2/\mathrm{s}$ (Fig. 2.2 b), the tendency of the swimmers to diffuse away from the surface is stronger, reducing the accumulation. The accumulation reaches 76% for $\alpha = 10$ continuing to increase slowly to 82% for $\alpha = 60$.

When chiral swimmers are considered ($\beta \neq 0$ and by extension $\Omega \neq 0$), the accumulation behavior is unchanged for smooth surfaces. In Fig. 2.2 (a,b), the green line shows the accumulation for $\Omega = 1$, which coincides with the blue diamonds for non-chiral swimmers ($\Omega = 0$). The chirality causes the swimmers to trace circular trajectories along the surface, but does not affect their overall surface accumulation.

2.2.2 Surface structured with convex obstacles

A very different behavior is observed, for both values of D_{R}, when randomly placed obstacles are added to the surface. We begin by considering swimmers with $D_{\mathrm{R}} = 10^{-4}\ \mathrm{rad}^2/\mathrm{s}$.

For non-chiral and chiral swimmers in a volume bounded by surfaces with obstacle surface density $\rho = 20\%$, the accumulation near the surfaces (lines with circles in Fig. 2.2 a) is reduced for all α for $\Omega < 1$ and for $\alpha \leq 10$ for $\Omega \geq 1$. Fig. 2.2 (c) shows the fraction $\frac{\phi}{\phi_0}$ of accumulated swimmers with angular velocity Ω near a surface with obstacles ϕ with respect to that of swimmers with the same angular velocity near a smooth surface ϕ_0, as a function of the alignment force α and angular velocity Ω.

For non chiral swimmers and chiral swimmers with $0 \leq \Omega \leq 1$, the reduction of the surface accumulation by the obstacles ($\frac{\phi}{\phi_0} < 1$ in Fig. 2.2 c) is a result of the modified surface structure. In the absence of an alignment force ($\alpha = 0$), about 8% of the swimmers accumulate at the surface. This accumulation is a result of the persistent motion of the swimmers, and the decrease in accumulation relative to the smooth surface can be attributed to the reduction of the flat surface area available to swimmers, because of the presence of obstacles. For $\alpha > 0$, when approaching an obstacle, a swimmer aligns its direction of motion along the convex boundary of the obstacle, instead of the surface plane, so that its orientation is directed away from the surface. As α is increased, the tendency to align along the surface or boundary of an obstacle becomes stronger, increasing the surface accumulation. A schematic trajectory that leaves the surface after aligning along an obstacle is shown for a non-chiral swimmer in Fig. 2.1 (a,II)

and a chiral swimmer in Fig. 2.1 (b,II). For $0 \leq \Omega < 1$ the accumulation increases with the angular velocity (Fig. 2.2 a). This can be explained by the chiral swimmers exploring the surface less extensively, thereby encountering fewer obstacles when compared to less chiral swimmers. As the angular velocity increases, the swimming orbits become smaller, decreasing the efficiency with which the surface is explored. This limits the ability of the obstacles to reduce the accumulation at the surface and leads to an increase of $\frac{\phi}{\phi_0}$ with the angular velocity in Fig. 2.2 (c).

For chiral swimmers with a larger angular velocity ($\Omega \geq 1$) a different behavior is observed, where swimmers move in persistent orbits along the boundary of an obstacle, until the rotational diffusion directs them away from the obstacle and they escape. A schematic example trajectory of a swimmer that orbits an obstacle is displayed in Fig. 2.1 (b, III). For $D_{\mathrm{R}} = 10^{-4}\ \mathrm{rad}^2/\mathrm{s}$, the rotational diffusion is relatively weak and the swimmers can become effectively trapped at the obstacles for a sufficiently strong alignment force $\alpha \geq 20$, increasing the surface accumulation in Fig. 2.2 (a). We note that due to this "orbital trapping", the ability of the obstacles to direct swimmers away from the surface is mitigated for $\alpha \geq 20$, whereby obstacles will rather enhancing surface accumulation ($\frac{\phi}{\phi_0} > 1$ in Fig. 2.2 c).

The trapping of a swimmer in an orbit around an obstacle is a result of the interplay between the angular velocity and the alignment force along the boundary of the obstacle. When a swimmer approaches an obstacle, the alignment force will guide the swimmer around its boundary. For a swimming orbit that is equal to the size of the obstacle ($\Omega = 1.0$), this results in a circular trajectory centered in the obstacle. When the swimming orbit is of the size, or smaller than the size of the obstacle, ($\Omega \geq 1$), the angular velocity will continuously direct the swimmer towards the centre of the obstacle with the alignment force directing the swimmer back along the boundary. A larger angular velocity will result in a stronger tendency to align along the boundary. Detachment of a swimmer from an orbit can occur when the Brownian diffusion is effective in reorienting the swimmer to escape from its orbit.

For $D_{\mathrm{R}} = 0.1\ \mathrm{rad}^2/\mathrm{s}$, the larger diffusion randomizes the motion, increasing the boundary detachment and reducing surface accumulation (Fig. 2.2 b). By perturbing the circular trajectories the diffusion increases the surface exploration of chiral swimmers, reducing the difference between different angular velocities Ω. Due to enhanced surface exploration, obstacles become more effective in reducing near surface accumulation of chiral swimmers, decreasing $\frac{\phi}{\phi_0}$ in Fig. 2.2 (d) (when compared to $D_{\mathrm{R}} = 10^{-4}\ \mathrm{rad}^2/\mathrm{s}$, in Fig. 2.2 c) for all but $\alpha < 10$ when the

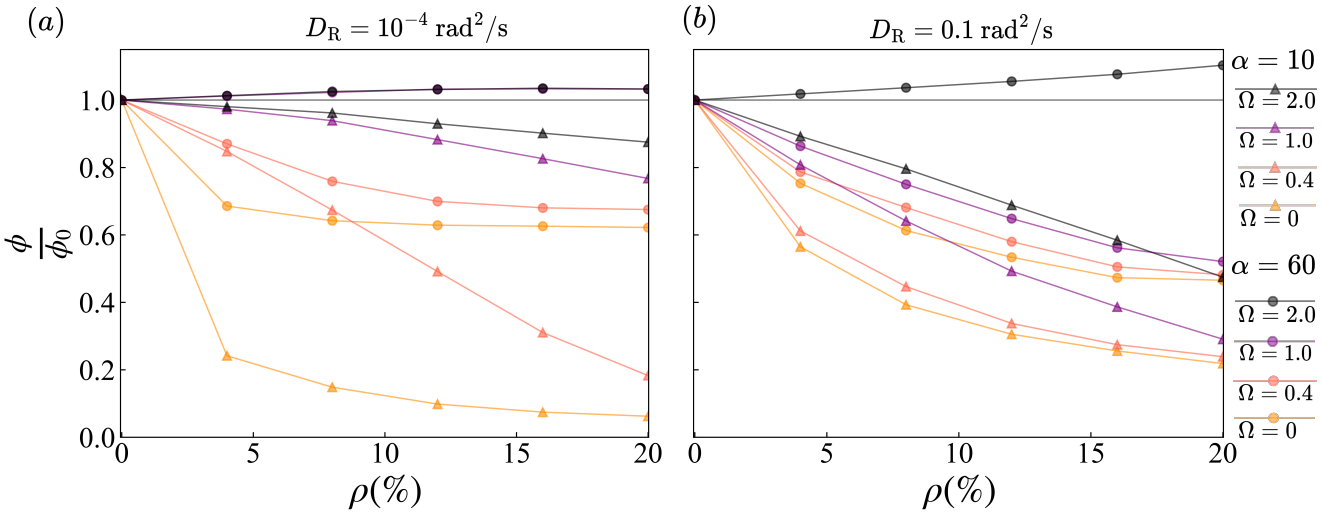

Figure 2.3: Fraction ϕ of swimmers accumulated near the surface for a given angular velocity Ω normalized to ϕ_0, the accumulation near a smooth surface for the same angular velocity, against the obstacles density ρ. The rotational diffusion is (a) $D_R = 10^{-4}$ rad^2/s and (b) $D_R = 0.1$ rad^2/s with alignment force strengths $\alpha = 10$ (triangles) and $\alpha = 60$ (circles).

alignment force is weak and diffusion dominates.

The effect of orbital trapping on surface accumulation is reduced significantly for most values of Ω. The diffusion breaks the orbits reducing the surface accumulation promoted by the obstacles ($\frac{\phi}{\phi_0} < 1$ in Fig. 2.2 d) with the exception of $\Omega = 2$, where the angular velocity is strong enough to keep the swimmer aligned along the boundary of an obstacle, effectively trapping it for $\alpha > 20$ ($\frac{\phi}{\phi_0} > 1$ in Fig.2.2 d).

2.2.3 Effect of the obstacle density on accumulation

Now we proceed to examine the effect of the obstacle density ρ. In Fig. 2.3 (a,b) $\frac{\phi}{\phi_0}$, the fraction of accumulated swimmers is presented for alignment force strengths $\alpha = 10$ (triangles) and $\alpha = 60$ (circles).

An increase in the density enhances the effect of the obstacles on the surface accumulation. The accumulation declines with increasing density for α and Ω where obstacles repel swimmers from the surface ($\frac{\phi}{\phi_0} < 1$ in Fig. 2.2 c,d) and increases where orbital trapping dominates the dynamics ($\frac{\phi}{\phi_0} > 1$ in Fig. 2.2 c,d).

As the angular velocity Ω increases, $\frac{\phi}{\phi_0}$ varies more weakly with the density in Fig. 2.3 (a,b). For swimmers with small angular velocities the accumulation declines rapidly for small densities before continuing to slowly decline. Due to the more efficient space exploration of swimmers with a small angular velocity, a lower density of obstacles is sufficient to affect

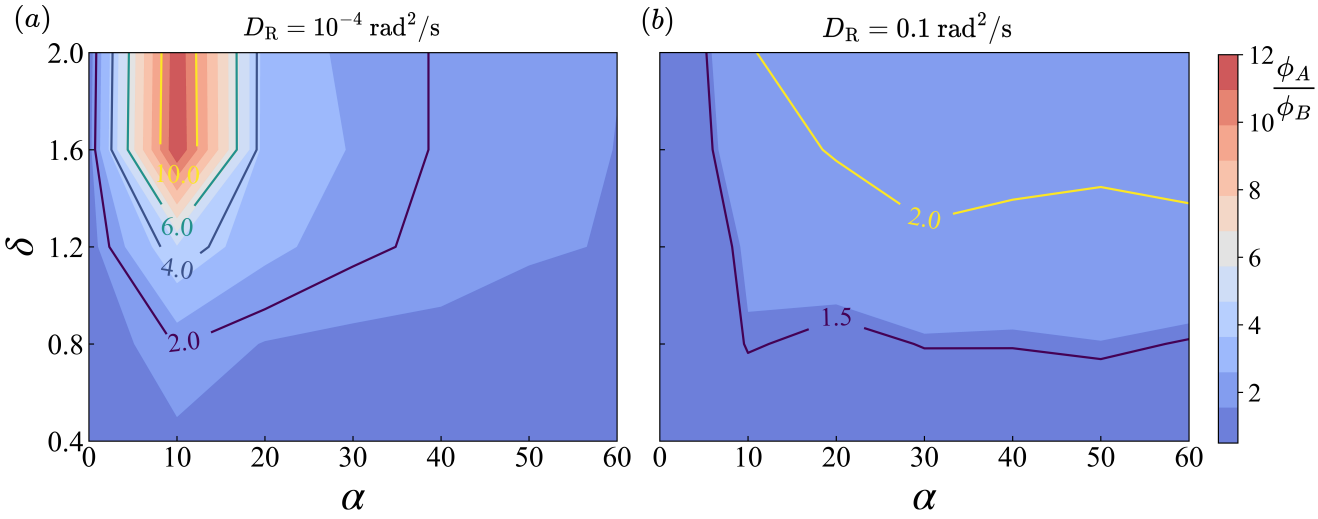

Figure 2.4: Separation efficiency $\frac{\phi_A}{\phi_B}$ of a mixture consisting of swimmers with chiralities Ω_A and Ω_B with accumulations ϕ_A and ϕ_B for two values of the rotational diffusion: (a) $D_R = 10^{-4}$ rad^2/s and (b) $D_R = 0.1$ rad^2/s. The separation efficiency is displayed as a function of the alignment force, α and the resolution of the separator, $\delta = \Omega_A - \Omega_B$.

the accumulation. This suggest that obstacles are effective in detaching swimmers with small angular velocities from the surface even at low densities. For swimmers with larger angular velocity, space exploration is less efficient, as increasing the density gradually increases the effect of the obstacles, and larger densities are required to affect the surface accumulation.

When we compare $D_R = 10^{-4}$ rad^2/s (Fig. 2.3 a) and $D_R = 0.1$ rad^2/s (Fig. 2.3 b), we note that for $D_R = 0.1$ rad^2/s increasing the obstacle density has a larger effect on $\frac{\phi}{\phi_0}$ for most values of the angular velocity Ω, suggesting that the density dominates the accumulation behavior.

2.2.4 Sorting swimmers by angular velocity

By controlling the accumulation of microswimmers, obstacles may be used to sort swimmers of different angular velocity [71–73]. Depending on the angular velocities, the swimmers will tend to accumulate near a surface or remain in the volume with a different probability. For simplicity we will assume that the swimmers in the mixture are identical in all aspects but their angular velocity and study the efficiency of the separation as a function of the alignment force and the different angular velocities of the mixture.

A way to sort swimmers of different angular velocities would be to consider obstacle sizes such that $\Omega < 1$ for one fraction (A) of swimmers and $\Omega > 1$ for the other (B). We define $\delta = \Omega_A - \Omega_B$ the resolution of the sorter and $\frac{\phi_A}{\phi_B}$ its efficiency. In Fig. 2.4 (a,b) the efficiency is

displayed for swimmers with $D_{\mathrm{R}} = 10^{-4}\ \mathrm{rad}^2/\mathrm{s}$ and $D_{\mathrm{R}} = 0.1\ \mathrm{rad}^2/\mathrm{s}$, for different values of the resolution δ and the alignment force strength α.

We observe that, as the rotational diffusion increases, the ability to sort the swimmers by angular velocity is reduced. For $D_{\mathrm{R}} = 10^{-4}\ \mathrm{rad}^2/\mathrm{s}$ (Fig. 2.4 a) the more chiral fraction accumulates up to 11 times as much as the less chiral one, whereas for $D_{\mathrm{R}} = 0.1\ \mathrm{rad}^2/\mathrm{s}$ (Fig. 2.4 b) the more chiral fraction accumulates by up to 2.5 times than the less chiral one.

For $D_{\mathrm{R}} = 10^{-4}\ \mathrm{rad}^2/\mathrm{s}$, and $\alpha \approx 10$ the fraction with a higher angular velocity accumulates significantly more than the other fraction and the mixture can be sorted, while for other α, the sorter becomes less efficient as α increases. For $D_{\mathrm{R}} = 0.1\ \mathrm{rad}^2/\mathrm{s}$ the alignment force strength needs to be above 20 for the two fractions to accumulate at different rates, and the sorter does not work efficiently.

2.3 Discussion

In this chapter, we introduced a 3D model to study the surface accumulation of a microswimmer, induced by steric forces and an effective short-ranged hydrodynamic force that aligns the propagation direction of the swimmer along the nearest boundary (surface or obstacle). Chiral and non-chiral microswimmers were considered, navigating a volume bounded by a bottom and a top surface plane. We introduced obstacles on the surfaces and studied their effect on the surface accumulation.

For smooth surfaces (without obstacles) and structured surfaces (with obstacles) the surface accumulation is enhanced by increasing the alignment force. The alignment force competes with diffusion to prevent the swimmer (chiral and non-chiral) from orienting away from the surface and escaping. When obstacles are added to the surface, the angular velocity of the swimmer is found to strongly affect their accumulation. For a non-chiral swimmer, the obstacles significantly reduce the accumulation when compared to a smooth surface, even when a small fraction of the surface is covered by obstacles. The obstacles prevent a swimmer from aligning with the surface, by guiding it away into the volume, consistent with recent experimental results [35]. For a chiral swimmer, the ability of obstacles to mitigate the accumulation is reduced with increasing angular velocity. Swimmers with a large angular velocity explore the surface less efficiently, encountering fewer obstacles, which reduces their effect. Moreover, for a chiral swimmer we find that for sufficiently strong alignment forces, the swimmer may be trapped in

a trajectory along the boundary of the obstacle [11,46,53], resulting in enhanced accumulation. We find that the relevant length scale for trapping is set by the obstacle size, such that as when the swimming orbit is of the size of the obstacle, or smaller, trapping can occur. We further note that, for swimmers that experience a stronger rotational diffusion, the motion becomes more randomized, reducing the effect of the angular velocity on the accumulation.

The ability of obstacles to impact the accumulation of microswimmers at a surface, may be used to guide the development of materials that selectively hinder or promote the adhesion of microswimmers, e.g., to control the establishment of biofilms in the case of bacteria. Our findings indicate that, by adding obstacles, for non-chiral swimmers, a surface can become more resistant to accumulation, which is in line with studies of bacterial accumulation [68]. For chiral swimmers, the way obstacles impact surface accumulation of microswimmers is more complex. Our findings suggest that, by selecting the size of the obstacles, we can control the accumulation near the surface. Covering a surface with obstacles could make it more resistant to the accumulation of microswimmers that are only weakly chiral (that swim in orbits larger than the size of the obstacles), but less resistant to strongly chiral swimmers (that swim in orbits with the size of the obstacle, or smaller).

Additionally, the surface accumulation of swimmers of different chiralities, or the tendency of swimmers to accumulate at obstacles that are larger than the radius of their swimming orbit, could be used to design a sorter of microswimmers based on their angular velocity. By selecting from a mixture of microswimmers the most appropriate swimming properties, the efficiency of microswimmers for a specific task e.g. drug-delivery or bioremediation may be improved [72, 73]. Alternatively, chirality-based spermatozoa selection may be employed to select cells with specific swimming traits desirable for artificial fertilization techniques [74]. Our results suggest that for chiral swimmers with a rotational diffusion similar to that of bull sperm, effective sorting by angular velocity could be achieved. Future work might include differently shaped obstacles that are known to trap swimmers well to further explore this idea.

In recent studies, for a microswimmer following a convex boundary, the angle between swimmer and boundary, was found to depend on the radius of curvature of the boundary [46,53]. By making the alignment force dependent on the radius of curvature we could explicitly include this in our model. Alternatively, in [20] the swimming behavior of an active particle between obstacles, resulting in optimal space exploration, was found to be different for convex and concave obstacles. In the future, the effect of cavities (or concave obstacles), in combination

with convex obstacles on surface accumulation of microswimmers could also be explored. In [20] the active particles were confined to a surface, while with the model proposed here would be possible to extend this study to 3D domains.

This chapter followed closely: DM van Roon, G Volpe, MMT da Gama, NAM Araújo, "3D model for surface accumulation of chiral and non-chiral microswimmers," arXiv:2401.05237.

Chapter 3

Conclusions

In the first chapter we examined numerically the effect of disorder in the steric interactions on the dynamics of a chiral active particle exploring a periodic arrangement of obstacles on a surface. By not considering explicitly hydrodynamic effects, we were able to study relatively complicated topographies including different arrangements, densities and sizes of obstacles. We were able to isolate the role of steric interactions and the effect of noise in these interactions, on the propagation of chiral active particles.

In the second chapter we introduced a model to study the dynamics of a microswimmer in a 3D volume bounded by a top and a bottom surface plane. Our model includes steric interactions and an effective, short-ranged, alignment force that aligns the propagation direction of the swimmer along the nearest boundary (surface or obstacle). The alignment force represented in an effective way, the short ranged hydrodynamic interaction between microswimmer and boundary and was able to reproduce well the near surface dynamics observed for *E. coli* and sperm cells. The simplicity of the effective interaction enabled us to investigate separately the role of hydrodynamic alignment and convex surface structure in the surface accumulation of microswimmers.

For microswimmers in two dimensions, many interesting phenomena, including commensuration effects in [48], topography dependent behavior to optimally explore space in [20, 21, 34], and confinement induced self-organisation in [19, 75, 76] have been observed. In the future, our model could be used to numerically explore further such behaviors in complex crowded 3D domains.

To study the surface accumulation of a specific type of microswimmer in detail, man-made or natural, the results of the model could be compared to experimental results to determine the

parameters that represent accurately the interaction of that microswimmer with a boundary. Alternatively, detailed hydrodynamic simulations of the swimmer approaching a boundary could be employed to determine realistic values for the parameters. Living microswimmers such as *E. coli*, in addition to Brownian noise, are known to be able to employ deliberate moves e.g. 'tumble moves' [21] to reorient their direction of motion towards or away from a wall. By including in a controlled way such organism specific moves in our model, we might be able to examine their role in space exploration or near surface accumulation, and better represent different organisms.

This thesis so far concerned individual microswimmers or 'dilute systems' in which the interactions between microswimmers were neglected. In their natural environment however, microswimmers often not only aggregate into colonies, swarms or biofilms, but also behave differently depending on the local density, as in quorum sensing. To study systems composed of many microswimmers, our models would have to be adapted to include these interactions. It would be necessary to verify whether the effective potentials in our models, which are based on experiments with dilute systems are still valid. This could be challenging, as it often is difficult to perform experiments with crowded systems. A further challenge is posed by the interpretation of experimental observations of such systems, to parameterize our models. To infer from macroscopic behavior the correct potential form that describes the interactions might be difficult. A first step could be to add steric interactions between swimmers, and to compare results to experimental findings. Such a comparison might provide us with cues to adapt our models. Subsequently short ranged (hydrodynamic) effects coupling the rotational degrees of freedom could be introduced. Alternatively, hydrodynamics simulations might be employed to shed light on the swimmer-swimmer interactions, but ultimately these would have to be compared to experiments too. This approach is likely to be limited to few interacting swimmers, as hydrodynamics simulations of large crowded systems tend to quickly become computationally unfeasible. By focusing on steric and effective short-ranged hydrodynamic interactions, we excluded the effects of possible long-ranged interactions. For systems with long-ranged effects e.g. chemo-taxis or alignment-interactions, our model is not expected to be adequate in its current form. In order to study such systems we would have to include these interactions in (an effective way) in our model.

In addition to a fundamental understanding of microswimmers in complex environments, our 3D model could be employed to guide the design of microfluidic chips that include mi-

croswimmers. A particular advantage of our model would be that it enables a quick numerical exploration of a design, before attempting to build it. A first concept could be a sorter of microswimmers based on their swimming properties. By placing pillars increasing size in a microfluidic channel, the scattering observed in [36–38] together with the dynamical trapping of microswimmers observed in [45, 46, 53] could be exploited. Further applications could include the development of micro-structured surfaces, that can control bacterial adhesion, limiting the growth of hazardous biofilms.

Bibliography

[1] S. Ramaswamy, "The mechanics and statistics of active matter," *Annual Review of Condensed Matter Physics*, vol. 1, no. 1, pp. 323–345, 2010.

[2] G. Gonnella, D. Marenduzzo, A. Suma, and A. Tiribocchi, "Motility-induced phase separation and coarsening in active matter," *Comptes Rendus Physique*, vol. 16, no. 3, pp. 316–331, 2015.

[3] G. Gompper, R. G. Winkler, T. Speck, A. Solon, C. Nardini, F. Peruani, H. Löwen, R. Golestanian, U. B. Kaupp, L. Alvarez, T. Kiørboe, E. Lauga, W. C. K. Poon, A. DeSimone, S. Muiños-Landin, A. Fischer, N. A. Söker, F. Cichos, R. Kapral, P. Gaspard, M. Ripoll, F. Sagues, A. Doostmohammadi, J. M. Yeomans, I. S. Aranson, C. Bechinger, H. Stark, C. K. Hemelrijk, F. J. Nedelec, T. Sarkar, T. Aryaksama, M. Lacroix, G. Duclos, V. Yashunsky, P. Silberzan, M. Arroyo, and S. Kale, "The 2020 motile active matter roadmap," *Journal of Physics: Condensed Matter*, vol. 32, no. 19, p. 193001, 2020.

[4] E. Lauga, W. R. DiLuzio, G. M. Whitesides, and H. A. Stone, "Swimming in circles: Motion of bacteria near solid boundaries," *Biophysical Journal*, vol. 90, no. 2, pp. 400–412, 2006.

[5] A. Bukatin, I. Kukhtevich, N. Stoop, J. Dunkel, and V. Kantsler, "Bimodal rheotactic behavior reflects flagellar beat asymmetry in human sperm cells," *Proceedings of the National Academy of Sciences*, vol. 112, no. 52, pp. 15904–15909, 2015.

[6] A. S. Utada, R. R. Bennett, J. C. N. Fong, M. L. Gibiansky, F. H. Yildiz, R. Golestanian, and G. Wong, "Vibrio cholerae use pili and flagella synergistically to effect motility switching and conditional surface attachment," *Nature Communications*, vol. 5, p. 4913, 2014.

[7] B. Liebchen and D. Levis, "Chiral active matter," 2022.

[8] C. Bechinger, R. Di Leonardo, H. Löwen, C. Reichhardt, G. Volpe, and G. Volpe, "Active particles in complex and crowded environments," *Reviews of Modern Physics*, vol. 88, no. 4, p. 045006, 2016.

[9] A. Callegari and G. Volpe, *Numerical Simulations of Active Brownian Particles*, pp. 211–238. 2019.

[10] J. R. Howse, R. A. L. Jones, A. J. Ryan, T. Gough, R. Vafabakhsh, and R. Golestanian, "Self-motile colloidal particles: From directed propulsion to random walk," *Physical Review Letters*, vol. 99, p. 048102, 2007.

[11] S. van Teeffelen and H. Löwen, "Dynamics of a brownian circle swimmer," *Physical Review Letters E*, vol. 78, p. 020101, 2008.

[12] L. Caprini and U. Marini Bettolo Marconi, "Active chiral particles under confinement: surface currents and bulk accumulation phenomena," *Soft Matter*, vol. 15, pp. 2627–2637, 2019.

[13] S. van Teeffelen, U. Zimmermann, and H. Löwen, "Clockwise-directional circle swimmer moves counter-clockwise in petri dish- and ring-like confinements," *Soft Matter*, vol. 5, pp. 4510–4519, 2009.

[14] F. J. Sevilla, "Diffusion of active chiral particles," *Physical Review Letters E*, vol. 94, p. 062120, 2016.

[15] M. P. Allen and D. J. Tildesley, *Computer Simulation of Liquids*. USA: Clarendon Press, 1989.

[16] "Front matter," in *Understanding Molecular Simulation (Third Edition)* (D. Frenkel and B. Smit, eds.), pp. i–iii, Academic Press, third edition ed., 2023.

[17] M. Reza Shaebani, A. Wysocki, R. Winkler, G. Gompper, and H. Rieger, "Computational models for active matter," 2019.

[18] A. C. Brańka and D. M. Heyes, "Algorithms for brownian dynamics computer simulations: Multivariable case," *Phys. Rev. E*, vol. 60, pp. 2381–2387, 1999.

[19] N. A. M. Araújo, L. M. C. Janssen, T. Barois, G. Boffetta, I. Cohen, A. Corbetta, O. Dauchot, M. Dijkstra, W. M. Durham, A. Dussutour, S. Garnier, H. Gelderblom, R. Golestanian, L. Isa, G. H. Koenderink, H. Löwen, R. Metzler, M. Polin, C. P. Royall, A. Šarić, A. Sengupta, C. Sykes, V. Trianni, I. Tuval, N. Vogel, J. M. Yeomans, I. Zuriguel, A. Marin, and G. Volpe, "Steering self-organisation through confinement," *Soft Matter*, vol. 19, pp. 1695–1704, 2023.

[20] G. Volpe and G. Volpe, "The topography of the environment alters the optimal search strategy for active particles," *Proceedings of the National Academy of Sciences*, vol. 114, no. 43, pp. 11350–11355, 2017.

[21] E. Perez Ipiña, S. Otte, R. Pontier-Bres, D. Czerucka, and F. Peruani, "Bacteria display optimal transport near surfaces," *Nature Physics*, vol. 15, pp. 1–6, 03 2019.

[22] J. Li, B. E. de Avila, W. Gao, L. Zhang, and J. Wang, "Micro/nanorobots for biomedicine: Delivery, surgery, sensing, and detoxification," *Science Robotics*, vol. 2, p. eaam6431, 2017.

[23] W. Gao and J. Wang, "The environmental impact of micro/nanomachines: a review," *ACS nano*, vol. 8, no. 4, pp. 3170–3180, 2014.

[24] J. Zhang, Z. Chen, R. K. Kankala, S.-B. Wang, and A.-Z. Chen, "Self-propelling micro-/nano-motors: Mechanisms, applications, and challenges in drug delivery," *International Journal of Pharmaceutics*, vol. 596, p. 120275, 2021.

[25] P. Erkoc, I. C. Yasa, H. Ceylan, O. Yasa, Y. Alapan, and M. Sitti, "Mobile microrobots for active therapeutic delivery," *Advanced Therapeutics*, vol. 2, p. 1800064, 2018.

[26] J. S. Adadevoh, S. C. Triolo, C. A. Ramsburg, and R. M. Ford, "Chemotaxis increases the residence time of bacteria in granular media containing distributed contaminant sources.," *Environmental science & technology*, vol. 50 1, pp. 181–7, 2016.

[27] G. Volpe, I. Buttinoni, D. Vogt, H.-J. Kümmerer, and C. Bechinger, "Microswimmers in patterned environments," *Soft Matter*, vol. 7, pp. 8810–8815, 2011.

[28] T. Mano, J.-B. Delfau, J. Iwasawa, and M. Sano, "Optimal run-and-tumble–based transportation of a janus particle with active steering," *Proceedings of the National Academy of Sciences*, vol. 114, no. 13, pp. E2580–E2589, 2017.

[29] M. A. Fernandez-Rodriguez, F. Grillo, L. Alvarez, M. Rathlef, I. Buttinoni, G. Volpe, and L. Isa, "Feedback-controlled active brownian colloids with space-dependent rotational dynamics," *Nature Communications*, vol. 11, no. 1, p. 4223, 2020.

[30] A. Dehkharghani, N. Waisbord, and J. S. Guasto, "Self-transport of swimming bacteria is impaired by porous microstructure," 2022.

[31] M. Zeitz, K. Wolff, and H. Stark, "Active brownian particles moving in a random lorentz gas," *The European Physical Journal E*, vol. 40, pp. 1–10, 2017.

[32] O. Chepizhko and T. Franosch, "Ideal circle microswimmers in crowded media," *Soft Matter*, vol. 15, pp. 452–461, 2019.

[33] O. Chepizhko and T. Franosch, "Random motion of a circle microswimmer in a random environment," *New Journal of Physics*, vol. 22, no. 7, p. 073022, 2020.

[34] D. M. van Roon, G. Volpe, M. M. Telo da Gama, and N. A. M. Araújo, "The role of disorder in the motion of chiral active particles in the presence of obstacles," *Soft Matter*, vol. 18, pp. 6899–6906, 2022.

[35] S. Makarchuk, V. Braz, N. Araujo, L. Ciric, and G. Volpe, "Enhanced propagation of motile bacteria on surfaces due to forward scattering," *Nature Communications*, vol. 10, p. 4110, 2019.

[36] A. T. Brown, I. D. Vladescu, A. Dawson, T. Vissers, J. Schwarz-Linek, J. S. Lintuvuori, and W. C. K. Poon, "Swimming in a crystal," *Soft Matter*, vol. 12, pp. 131–140, 2016.

[37] A. Weber, M. Bahrs, Z. Alirezaeizanjani, X. Zhang, C. Beta, and V. Zaburdaev, "Rectification of bacterial diffusion in microfluidic labyrinths," *Frontiers in Physics*, vol. 7, p. 148, 2019.

[38] M. Brun-Cosme-Bruny, E. Bertin, B. Coasne, P. Peyla, and S. Rafaï, "Effective diffusivity of microswimmers in a crowded environment," *The Journal of Chemical Physics*, vol. 150, no. 10, p. 104901, 2019.

[39] C. Kurzthaler, S. Mandal, T. Bhattacharjee, H. Löwen, S. Dattaf, and H. Stone, "A geometric criterion for the optimal spreading of active polymers in porous media," *Nature Communications*, vol. 12, no. 1, p. 7088, 2021.

[40] D. Clausznitzer and R. Endres, "Noise characteristics of the escherichia coli rotary motor," *BMC systems biology*, vol. 5, p. 151, 2011.

[41] M. Polin, I. Tuval, K. Drescher, J. P. Gollub, and R. E. Goldstein, "¡i¿chlamydomonas¡/i¿ swims with two “gears” in a eukaryotic version of run-and-tumble locomotion," *Science*, vol. 325, no. 5939, pp. 487–490, 2009.

[42] H. Löwen, "Inertial effects of self-propelled particles: From active brownian to active langevin motion," *The Journal of Chemical Physics*, vol. 152, no. 4, p. 040901, 2020.

[43] O. Dauchot and V. Démery, "Dynamics of a self-propelled particle in a harmonic trap," *Phys. Rev. Lett.*, vol. 122, p. 068002, 2019.

[44] D. Breoni, M. Schmiedeberg, and H. Löwen, "Active brownian and inertial particles in disordered environments: Short-time expansion of the mean-square displacement," *Phys. Rev. E*, vol. 102, p. 062604, Dec 2020.

[45] D. Takagi, J. Palacci, A. Braunschweig, M. Shelley, and J. Zhang, "Hydrodynamic capture of microswimmers into sphere-bound orbits," *Soft Matter*, vol. 10, pp. 1784–1789, march 2014.

[46] S. E. Spagnolie, G. R. Moreno-Flores, D. Bartolo, and E. Lauga, "Geometric capture and escape of a microswimmer colliding with an obstacle," *Soft Matter*, vol. 11, no. 17, p. 3396–3411, 2015.

[47] K. J. Modica, Y. Xi, and S. C. Takatori, "Porous media microstructure determines the diffusion of active matter: Experiments and simulations," *Frontiers in Physics*, vol. 10, p. 869175, 2022.

[48] C. Reichhardt and C. J. O. Reichhardt, "Active matter commensuration and frustration effects on periodic substrates," *Physical Review Letters E*, vol. 103, p. 022602, 2021.

[49] R. G. Crystal, S. H. Randell, J. F. Engelhardt, J. Voynow, and M. E. Sunday, "Airway epithelial cells: current concepts and challenges," *Proceedings of the American Thoracic Society*, vol. 5, no. 7, p. 772—777, 2008.

[50] N. P. Vizarim, C. J. O. Reichhardt, P. A. Venegas, and C. Reichhardt, "Skyrmion pinball and directed motion on obstacle arrays," *Journal of Physics Communications*, vol. 4, no. 8, p. 085001, 2020.

[51] A. P. Berke, L. Turner, H. C. Berg, and E. Lauga, "Hydrodynamic attraction of swimming microorganisms by surfaces," *Phys. Rev. Lett.*, vol. 101, p. 038102, 2008.

[52] G. Li and J. X. Tang, "Accumulation of microswimmers near a surface mediated by collision and rotational brownian motion," *Phys. Rev. Lett.*, vol. 103, p. 078101, Aug 2009.

[53] O. Sipos, K. Nagy, R. Di Leonardo, and P. Galajda, "Hydrodynamic trapping of swimming bacteria by convex walls," *Phys. Rev. Lett.*, vol. 114, p. 258104, Jun 2015.

[54] M. P. Schultz, J. A. Bendick, E. R. Holm, and W. M. Hertel, "Economic impact of biofouling on a naval surface ship," *Biofouling*, vol. 27, no. 1, pp. 87–98, 2011.

[55] G. D. Bixler and B. Bhushan, "Biofouling: lessons from nature," *Philosophical Transactions of the Royal Society A: Mathematical, Physical and Engineering Sciences*, vol. 370, no. 1967, pp. 2381–2417, 2012.

[56] J. Fiedler, A. Kolitsch, B. Kleffner, D. Henke, S. Stenger, and R. E. Brenner, "Copper and silver ion implantation of aluminium oxide-blasted titanium surfaces: Proliferative response of osteoblasts and antibacterial effects," *The International Journal of Artificial Organs*, vol. 34, no. 9, pp. 882–888, 2011.

[57] G. Kang and Y. Cao, "Development of antifouling reverse osmosis membranes for water treatment: A review," *Water Research*, vol. 46, no. 3, pp. 584–600, 2012.

[58] Z. Khatoon, C. D. McTiernan, E. J. Suuronen, T.-F. Mah, and E. I. Alarcon, "Bacterial biofilm formation on implantable devices and approaches to its treatment and prevention," *Heliyon*, vol. 4, no. 12, p. e01067, 2018.

[59] P. S. Leonov, X. Flores-Alsina, K. V. Gernaey, and C. Sternberg, "Microbial biofilms in biorefinery – towards a sustainable production of low-value bulk chemicals and fuels," *Biotechnology Advances*, vol. 50, p. 107766, 2021.

[60] J. Gadkari, S. Bhattacharya, and A. Shrivastav, "Chapter 7 - importance and applications of biofilm in microbe-assisted bioremediation," in *Development in Wastewater Treatment Research and Processes* (M. P. Shah, S. Rodriguez-Couto, and R. T. Kapoor, eds.), pp. 153–173, Elsevier, 2022.

[61] M. Dade-Robertson, A. Keren-Paz, M. Zhang, and I. Kolodkin-Gal, "Architects of nature: growing buildings with bacterial biofilms," *Microbial Biotechnology*, vol. 10, no. 5, pp. 1157–1163, 2017.

[62] Y. Luan, S. Liu, M. Pihl, H. van der Mei, J. Liu, F. Hizal, C.-H. Choi, H. Chen, Y. Ren, and H. Busscher, "Bacterial interactions with nanostructured surfaces," *Current Opinion in Colloid and Interface Science*, vol. 38, pp. 170–189, 2018.

[63] J. Shi, S. Wang, X. Cheng, S. Chen, and G. Liu, "Constructing zwitterionic nanofiber film for anti-adhesion of marine corrosive microorganisms," *Journal of Materials Science Technology*, vol. 70, pp. 145–155, 2021.

[64] S. B. Chinnaraj, P. G. Jayathilake, J. Dawson, Y. Ammar, J. Portoles, N. Jakubovics, and J. Chen, "Modelling the combined effect of surface roughness and topography on bacterial attachment," *Journal of Materials Science Technology*, vol. 81, pp. 151–161, 2021.

[65] S. Bianchi, F. Saglimbeni, and R. Di Leonardo, "Holographic imaging reveals the mechanism of wall entrapment in swimming bacteria," *Phys. Rev. X*, vol. 7, p. 011010, 2017.

[66] S. Bianchi, F. Saglimbeni, G. Frangipane, D. Dell'Arciprete, and R. Di Leonardo, "3d dynamics of bacteria wall entrapment at a water–air interface," *Soft Matter*, vol. 15, pp. 3397–3406, 2019.

[67] K. Drescher, J. Dunkel, L. H. Cisneros, S. Ganguly, and R. E. Goldstein, "Fluid dynamics and noise in bacterial cell–cell and cell–surface scattering," *Proceedings of the National Academy of Sciences*, vol. 108, pp. 10940 – 10945, 2011.

[68] K. Yang, J. Shi, L. Wang, Y. Chen, C. Liang, L. Yang, and L.-N. Wang, "Bacterial anti-adhesion surface design: Surface patterning, roughness and wettability: A review," *Journal of Materials Science Technology*, vol. 99, pp. 82–100, 2022.

[69] G. Li and J. X. Tang, "Accumulation of microswimmers near a surface mediated by collision and rotational brownian motion," *Phys. Rev. Lett.*, vol. 103, p. 078101, 2009.

[70] G. M. Whitesides, E. Ostuni, S. Takayama, X. Jiang, and D. E. Ingber, "Soft lithography in biology and biochemistry," *Annual Review of Biomedical Engineering*, vol. 3, no. 1, pp. 335–373, 2001.

[71] T. Laird, “Chiral separation methods for pharmaceutical and biotechnological products,” *Organic Process Research & Development*, vol. 15, no. 4, pp. 946–946, 2011.

[72] M. Mijalkov and G. Volpe, “Sorting of chiral microswimmers,” *Soft Matter*, vol. 9, pp. 6376–6381, 2013.

[73] Marcos, H. C. Fu, T. R. Powers, and R. Stocker, “Separation of microscale chiral objects by shear flow,” *Physical Review Letters*, vol. 102, no. 15, 2009.

[74] I. Oseguera-López, S. Ruiz-Díaz, P. Ramos-Ibeas, and S. Pérez-Cerezales, “Novel techniques of sperm selection for improving ivf and icsi outcomes,” *Frontiers in Cell and Developmental Biology*, vol. 7, 2019.

[75] M. D. Neto, M. B. Oliveira, and J. F. Mano, “Microparticles in contact with cells: From carriers to multifunctional tissue modulators,” *Trends in Biotechnology*, vol. 37, no. 9, pp. 1011–1028, 2019.

[76] D. Richter and M. Kruteva, “Polymer dynamics under confinement,” *Soft Matter*, vol. 15, pp. 7316–7349, 2019.